Design and Implementation of a Stepped Frequency Continuous Wave Radar System for Biomedical Applications

A Thesis Presented for the

Master of Science

Degree

The University of Tennessee, Knoxville

Sabikun Nahar
August 2018

Copyright © 2018 by Sabikun Nahar
All rights reserved.

Dedicated to my parents and my husband

ACKNOWLEDGEMENTS

I would first like to thank my thesis advisor Dr. Aly E. Fathy of the Department of Electrical Engineering and Computer Science at University of Tennessee, Knoxville. As my teacher and mentor, he has taught me more than I could ever give him credit for. Through sharing his expertise and extensive insight in the field of microwave circuits and antennas, Professor Fathy made working on this project an extraordinarily fulfilling and enjoyable experience.

Besides my supervisor, I would like to thank the rest of my thesis committee: Dr. Teja Kuruganti, and Prof. Seddik M. Djouadi. They have both put their valuable time and effort to guide me through this process.

This work would not have been possible without the financial support of Maxentric Technologies, so my sincere gratitude goes out to them as well.

Finally, I have to express heartfelt gratefulness to my parents and my spouse for providing me with continuous encouragement and unwavering support throughout my educational life. They have always motivated me to pursue my goals and this accomplishment could never be achievable without them.

ABSTRACT

There is a need to detect vital signs of human (e.g., the respiration and heart-beat rate) with noncontact method in a number of applications such as search and rescue operation (e.g. earthquakes, fire), health monitoring of the elderly, performance monitoring of athletes Ultra-wideband radar system can be utilized for noncontact vital signs monitoring and tracking of various human activities of more than one subject. Therefore, a stepped-frequency continuous wave radar (SFCW) system with wideband performance is designed and implemented for Vital signs detection and fall events monitoring. The design of the SFCW radar system is firstly developed using off-the-shelf discrete components. Later, the system is implemented using surface mount components to make it portable with low cost. The measurement result is proved to be accurate for both heart rate and respiration rate detection within ±5% when compared with contact measurements. Furthermore, an electromagnetic model has been developed using a multi-layer dielectric model of the human subject to validate the experimental results. The agreement between measured and simulated results is good for distances up to 2 m and at various subjects' orientations with respect to the radar, even in the presence of more than one subject. The compressive sensing (CS) technique is utilized to reduce the size of the acquired data to levels significantly below the Nyquist threshold. In our demonstration, we use phase information contained in the obtained complex high-resolution range profile (HRRP) to derive the motion characteristics of the human. The obtained data has been successfully utilized for non-contact walk, fall and limping detection and healthcare monitoring. The effectiveness of the proposed method is validated using measured results.

TABLE OF CONTENTS

Chapter One Introduction....1
1.1 Motivations....2
1.2 Radar Theory....3
1.3 State of the Art in Vital Signs Radar....5
1.4 Scope of the Thesis....7
Chapter Two System Development of SFCW Radar....8
2.1 Design Considaration....8
2.1.1 Signal Generation....8
2.1.2 Operating Frequency....10
2.2 Design Parameters....11
2.3 System Description....14
2.3.1 Single Channel System....14
2.3.2 Multi Channel System....15
2.3.3 Link Budget Analysis of Two Channel System....17
2.3.4 Compact Proposed Radar System....18
2.4 Conclusion....22
Chapter Three An Electromagnetic Model of Human Vital Signs Detection and It's Experimental Validation....23
3.1 Background....23
3.2 Electromagnetic Model....24
3.3 Phase Based Methods....28
3.4 Experimental Validation....31
3.4.1 Subject at different orientations....31
3.4.2 Subject at different distances....34
3.4.3 Subject lying down on ground....35
3.4.4 Multiple subjects in the scene....36
3.4.5 Effect of transversal distance between subjects....38
3.4.6 Effect of longitudinal distance between subjects....39
3.5 Discussion....41
3.6 Conclusion....41
Chapter Four Alternatives to Big Data Acquisition Using Stepped Frequency Continuous Wave Radar and Compressive Sensing Algorithms....43
4.1 Background....43
4.2 Compressive Sensing Algorithm....46
4.3 Full-wave Electromagnetic Scattering Model....49
4.4 Fall Detection Analysis....50
4.4.1 Standing and Walking....51
4.4.2 Limping....52
4.4.3 Falling on the ground....52
4.5 Conclusion....54
Chapter Five Summary of Work....55
5.1 Future Work....57

List of References 58
Appendix 64
Vita 72

LIST OF TABLES

Table 1.1. State-of-the-art research comparison.....6

Table 2.1. Dielectric Properties of Various Building Materials.....10

Table 2.2. System Design Parameters. 13

Table 2.3. Components used in integrated transmitter. 20

Table 2.4. Components used in integrated receiver.....21

Table 3.1. Comparison between different radar technologies..…..24

Table 3.2. Simulated torso dimensions in normal respiration.…..26

Table 3.3. Thickness, dielectric constant information of human body parts at different frequencies and their corresponding effective dielectric constant..27

Table 3.4. The respiratory rates and heart rates from the contact sensors and simulated and measured radar results for the four different orientations.. ...32

Table 3.5. Error percentages for different distances.. 35

Table 3.6. Error percentage for detecting vital signs for a lying down subject.. ..36

Table 3.7. Error percentage for detecting vital signs for two subjects... 37

Table 3.8. Error percentage for detecting respiration for two subjects with different transversal distances.. 39

Table 3.9. Error percentage for detecting respiration for two subjects with different longitudinal distances.....40

Table 3.10. Comparison of the proposed SFCW Radar performance with other state-of-the-art.. 42

Table 4.1. Various methods of non-contact fall detection and their disadvantage.. 45

LIST OF FIGURES

Figure 1.1. Different target applications of the proposed radar based human sensing system: (a) Search and rescue operation in an earthquake scenario, (b) Vital signs monitoring of infants with sensitive skin conditions, (c) Continuous elderly monitoring and (d) Apnea detection for premature infants.. 2

Figure 2.1. Step-frequency waveform generation in the time domain. 8

Figure 2.2. Signal Generator Based on DDS-Driven PLL Architecture.. 9

Figure 2.3. Simulated through wall reflection and transmission through various building materials. 10

Figure 2.4. Top-level block diagram of the single channel SFCW radar system... 14

Figure 2.5. Single channel implemented system of SFCW radar. 15

Figure 2.6. Block diagram of two channel SFCW radar.. 16

Figure 2.7. Block diagram of four channel SFCW radar.....16

Figure 2.8. Link Budget analysis of transmitter.. 17

Figure 2.9. Link Budget analysis of receiver.. 18

Figure 2.10. Stack-up SFCW radar system.. 19

Figure 2.11. SFCW Radar Stack-up Implementation.. 19

Figure 2.12. The fabricated FR4 board of the transmitter.. 20

Figure 2.13. The fabricated board of the receiver. 21

Figure 2.14. Stack-up implementation of two-channel SFCW radar system.... ...22

Figure 3.1. Human Torso Model Geometry.....25

Figure 3.2. (a) Inhomogeneous medium of different dielectric layers. (b) Equivalent homogenous model.. 26

Figure 3.3. Proposed phase based methods.. 28

Figure 3.4. Steps of phase-based method to detect vital signs.....30

Figure 3.5. Subject at different angles. Ref 00, (1) 450, (2) 900, (3) -450.....32

Figure 3.6. The breathing rate and heart beat based on: (a) simulated data (b) measurement for subject in different orientations.....33

Figure 3.7. Subject at different distances (a) 1m, (b) 3m.. 34

Figure 3.8. The breathing rate and heart beat based on simulated and measured data... 34

Figure 3.9. Person under test is lying on ground.. 35

Figure 3.10. Simulation and measurement results for person under test lying on the ground.....36

Figure 3.11. The vital sings spectrum showing respiration and heart rate for (a) 1st person. (b) 2nd person... 37

Figure 3.12. Setup of two human beings under test where the transversal distance between them is variable... 38

Figure 3.13. Extracted time domain respiration signal from radar data for two distances showing the effect of spacing between the two subjects... 39

Figure 3.14. Setup of two human beings under test where the transversal distance between the subjects are varied ... .40

Figure 3.15. Detection of displacement due to vital signs detected by radar... ...40

Figure 4.1. Fall detection monitoring using (a) conventional method and (b) compressive sensing... 47

Figure 4.2. Human body (a) Human model with 17 joints, (b) Human models with 16 ellipsoids and (c) Meshed human body... 49

Figure 4.3. When subject walking, the instantaneous velocity acquired with simulation, conventional method and CS.....51

Figure 4.4. The velocity of the target limping obtained from experimental data and simulation.....52

Figure 4.5. The velocity of the subject falling on mattress from a standing position obtained from experimental data (conventional/full set and CS) and from simulation.....53

Figure 4.6. The target falling on a mattress from a standing position obtained from experimental data (conventional and CS) and from simulation, (a) acceleration, and (b) from experimental data using conventional method and CS.....53

Figure 4.7. (a) HRRP for walking, (b) HRRP for limping, (c) HRRP for falling, (d) Walking HRRP using CS, (e) Limping HRRP using CS, (f) Falling HRRP using CS…….....54

Figure A.1.1. The block diagram of a DDS, illustrating the output of each stage..66

Figure A.1.2. A photograph of the two-channel DDS board……..…...66

Figure A.2.1. The general process of MLFMA……...68

Figure A.3.1. Human motions: standing still and then falling on knee……..…70

Figure A.3.2. Human motions: standing still and then walking……71

Figure A.3.3. Human motions: standing still and then limping……71

CHAPTER ONE

INTRODUCTION

Remote monitoring technology has improved remarkably over the past few decades. This technology especially in healthcare has great advantages of emphasizing early detection and prevention of disorders as well as personalized health management [1, 2]. Remote detection of human subjects' vital signs technology is even more significant in case of rescue operations and for non-contact motion detection for elderly. For example, the injuries sustained from fall incidents are very serious for elderly subjects and monitoring their activities can help in getting care rapidly and eventually prevent such events. According to [3,4], there is a great importance of ubiquitous care for patients' health remotely that can extend patient care from hospital to home.

One of the popular examples of remote monitoring is regular vital signs recording. It can benefit the prediction, prevention and treatment of a variety of health issues. There are many conventional contact sensing methods and technologies behind the vital signs monitoring including electrocardiogram (ECG), phonocardiograph (PCG) and inductive plethysmography. However, the drawbacks of these contact measurements are causing disturbance to the patient like skin irritations and discomfort and also they are not feasible for unobtrusive long term monitoring. Unlike the aforementioned contact-based methods, noncontact vital signs monitoring, in particular, offers an attractive solution nowadays using ultra-wide band (UWB) radar system. Lately, the UWB remote monitoring systems have been advanced to track multiple vital signs such as heart rate (HR), respiratory rate (RR), electrocardiogram (ECG), blood pressure (BP), blood oxygen saturation (SpO2), blood glucose (BG) concentrations and many more [1–4].

In this thesis, a stepped-frequency continuous wave (SFCW) radar system is implemented for remote monitoring of vital signs of human applications. Here the focus is on the technology and device implementation for vital signs detection and fall detection. The system utilizes the phase information for the signal processing to derive the tiny vibrations of the chest and the motion pattern of a subject. The main thrust in developing the SFCW is to provide a light-weight, low-cost system targeting biomedical applications or rescue operations. The design and construction of the SFCW radar have been experimentally tested and results have been validated using Electromagnetic (EM) model.

In the following, at first, the motivation behind developing the SFCW radar will be presented in section 1.1. In section 1.2, some radar theory will be presented. Section 1.3 will discuss the state of the art in the field of research on the UWB radar system, and the scope of the thesis will be introduced in section (1.3).

1.1 Motivations

Wireless technology has recently emerged as an enabler for remote monitoring revolution and could impact disease prediction, treatment, and prevention in home and clinical environments. In many applications such as in search and rescue operations in disaster areas, remote soldier health monitoring in battlefields, vital signs monitoring of infants and burn victims, use of contact sensors is just not a realistic option. In addition, for applications that require continuous monitoring, such as fall detection in elder homes and sleep apnea monitoring for premature infants, wearing or attaching contact sensors on the body is inconvenient and impractical. The motivation of this thesis work is to provide an elegant, accurate and portable solution to this problem through the use of microwave radars. The goal was to come up with a system capable of fully monitoring vital signs for general health follow-ups and understand the different kinematics of human motions for many applications such as aiding elderly, gait analysis and fall detection.



(a) (b)

(c) (d)

Figure 1.1. Different target applications of the proposed radar based human sensing system: (a) Search and rescue operation in an earthquake scenario, (b) Vital signs monitoring of infants with sensitive skin conditions, (c) Continuous elderly monitoring and (d) Apnea detection for premature infants.

The non-contact cardiorespiratory monitor based on UWB technology provides truly remote, non-contact vital signs monitoring solution. It is especially useful for conditions that can be influenced or deteriorated by contact sensors, including neonatal monitoring, burn or trauma patient monitoring, sleep monitoring and so on. Additionally, monitoring and tracking of elderly's activities is becoming a great concern for health industry and the public. Fall detection, in particular, is considered to be a major public health problem, as a fall would usually result in a serious disability for elderly. Studies show that rapid detection of a fall event and immediate assistance after a fall can greatly reduce the adverse effects on the elderly [5]. Therefore, it is of great importance to develop a way to detect a fall automatically by using non-contact methods, and to report the fall incident to the related medical personnel so that proper care can be provided immediately. However better hardware and improved algorithms are required for robustness requirements.

In this thesis, stepped frequency continuous wave radar has been designed based on the discretization of the spectrum rather than using a continuous spectrum like in FM or impulse UWB radars. Use of UWB signal provides ranging and multi-person detection capabilities. But at the same time, the stepped frequency technique eliminates the need for high speed and expensive ADCs while maintaining easier calibration requirements. The implemented radar system operates with a center frequency of 3 GHz, with a 2 GHz bandwidth and a 20 MHz frequency step is utilized to detect the vital signs of human. The received baseband signal are processed using sophisticated signal processing schemes to extract vital signs or detect fall incidents of the subject.

1.2 Radar Theory

Radar technology has become prominent since the beginning of the 20th century. The principle of Radar is very similar to sound. It uses electromagnetic waves that is transmitted to the object and gets reflected from the object of interest. This returned energy is called an echo. Radar sets can use the echo to determine various information such as the direction, distance and velocity of the reflecting object. Radar functions similarly and is most commonly employed to obtain the location of a moving object through the use of radio frequency (RF) waves rather than sound.

To understand the principle of the radar system operation, it is important to understand the radar fundamental theory. Radar systems transmit microwave signals, which can either be a single tone or a pulse, through space with the speed of light. When the signal is intercepted by an obstacle, the signal is reflected off the object back to the radar. The reflection of the signal can be in towards any direction and but only the part that is captured by the receiving antenna is of

interest to the radar system. The radar system then analyzes the differences between the original transmitted signal and the reflected signal to provide useful information such as distance (based on the time delay between transmission and reception), size (based on the signal intensity), and velocity (based on phase and Doppler shift) of an object with respect to the radar system.

For a radar system with transmitted power of P_t, the directional power density at distance R is given by:

$$S_t = \frac{P_t}{4\pi R^2} \times G \tag{1-1}$$

Where G is the antenna gain. The reflected power is a function of this power density and the radar cross section (RCS). The radar cross section (RCS) of a radar system is the measure of the ratio of back scattered power density in the direction of the radar to the power density that is intercepted by the target. Since the scattered power is distributed on a shape of a sphere, a small part of this ($4\pi r^2$) can be received by the radar. The formula of the RCS can be defined as

$$\sigma = \frac{4\pi R^2 |E_R|^2}{|E_i|^2} \tag{1-2}$$

where E_R is electric field strength at range R and E_t is the electric field strength incident on the target. So the reflected power is then given by:

$$P_{ref} = S_t \times \sigma = \frac{P_t}{4\pi R^2} \times G \times \sigma \tag{1-3}$$

The power received by the radar is a function of this reflected power and effective antenna aperture, which can be defined as:

$$A_W = \frac{G\lambda^2}{4\pi} \tag{1-4}$$

where λ is the wavelength. Thus, the received power is given by:

$$P_{rec} = \frac{P_{ref}}{4\pi R^2} \times A_W = \frac{P_t . G^2 . \sigma . \lambda^2}{(4\pi)^3 R^4} \tag{1-5}$$

Which in turn gives the range of the subject through the classic radar equation:

$$R = \sqrt[4]{\frac{P_t . G^2 . \sigma . \lambda^2}{P_{rec}(4\pi)^3}} \tag{1-6}$$

In this thesis, a stepped-frequency continuous wave radar (SFCW) system has been designed, implemented and tested. SFCW radar transmitter set transmits a

discrete number of single tones continuously increasing by a constant frequency step. The mathematical expression of the transmitted stepped-frequency signal at frequency f_0 can be written as

$$S(t) = A_t \sin[2\pi(f_0 + n\Delta f)t] \tag{1-7}$$

The reflected signal from a subject can be represented as

$$S(t) = A_r \sin[\{2\pi(f_0 + n\Delta f)t\} - \phi(t) \tag{1-8}$$

Where A_r is the amplitude of the received signal, and $\phi(t)$ is the phase. The maximum unambiguous range can be formulated as

$$R_{amb} = \frac{c}{2\Delta f} \tag{1-9}$$

Another important parameter of the SFCW radar is range resolution which is the ability of a radar system to distinguish between two or more targets on the same bearing but at different ranges. The theoretical range resolution of a SFCW radar system can be calculated as

$$S_R = \frac{\mathrm{c}}{2B} \tag{1-10}$$

where B is the effective bandwidth and the c is the speed of light.

1.3 State of the Art in Vital Signs Radar

Various types of radars can be utilized for human sensing applications, like the continuous wave (CW) Doppler radar, ultra-wide band impulse radar, and stepped-frequency continuous wave (SFCW) or frequency-modulated continuous wave (FMCW) radar. CW radars have been used for remote vital signs detection [6-11], precise assessment of key cardiopulmonary activity parameters [12], motion or gesture sensing [13-15]. The big disadvantage of the CW radar is its inability to provide range information and conduct multi-person experiments. The UWB impulse radar can overcome that drawback through its use of narrow pulse and wide band signal. In order to provide cardio-respiratory estimation with high accuracy, various UWB radar systems have been proposed [16-21]. The feasibility of utilizing UWB radar system has also been demonstrated in the health care applications such as the ones presented in [16-19]. But, typically impulse radars need high-speed ADCs which are very expensive.

FMCW and SFCW radars on the other hand can eliminate this high-speed ADC requirement while still providing the advantage of the effective wide bandwidth.

FMCW radars have been successfully applied to non-contact vital signs detection and subject localization [22-24, 29]. But FMCW radars are typically more difficult to calibrate than the SFCW radars. SFCW radars can also skip certain frequency steps while maintaining the same level of performance through compressive sensing techniques which can speed-up the data collection process. These radars have also been widely studied for applications such as vital signs monitoring, gait analysis, and subject localization [25-28].

Below is a summary of the state-of-the-art research on SFCW and FMCW radars in this application. Since the operating principles of the UWB impulse radars are very different compared to these radars, they were not included in this table.

Table 1.1. State-of-the-art research comparison

Research Group	Radar Type	Application	Frequency Range	Accuracy
Peng et al. [29] 2017	FMCW + CW	Localization, ISAR Imaging, HR/RR	5.64-5.96 GHz	-
L. Qiu et al. [26] 2017	SFCW	Through wall life signal extraction	2.15–2.75 GHz	-
Wang et al. [23] 2015	FMCW	HR/RR	75-85 GHz	8%
Ren et al. [27] 2015	SFCW	HR/RR	3.14-3.46 GHz	5.7%
Wang et al. [22] 2014	FMCW/CW	HR/RR	5.72-5.88 GHz	-
Wang et al. [24] 2014	FMCW	RR	5.72-5.88 GHz	-
Liu et al. [28] 2014	SFCW	RR	0.3-1.3 GHz	-

1.4 Scope of the Thesis

In this thesis, SFCW radar system has been introduced with off-the-shelf components initially. Later the system was implemented with respective ICs to make it portable. Finally, this system is utilized for monitoring vital signs and fall events of elderly people during the validation phases. There are three objectives identified for this project:

i. To design and implement a SFCW radar system
The SFCW radar system design is simple and straight forward. Simple, light weight, compact, and low-cost design are the overall top-level requirements. The proposed system can achieve wide bandwidth using multi-channel implementation. In this thesis, the SFCW radar is designed 2 GHz bandwidth which is suitable for many biomedical applications.

ii. To validate the SFCW radar performance
For the experimental validation, two different tests were performed using SFCW radar system. One of them is vital signs detection. During the experiments, a standard pulse sensor and respiratory contact sensor are used to record the heartbeat and breathing rates and are used as the ground truth. The second test is used for fall detection analysis. The distinct events that are considered here in this research are regular activities such as standing and walking, limping and falling on a mattress.

iii. To Simulate Human Model
Firstly, a human rib cage was modeled using an elliptical cylinder with the appropriate dimensions. Then an inhomogeneous model of the rib-cage was created that consisted of different layers with different dielectric constants to represent the skin, the bones, muscles, fat, blood and so on. These modeling efforts were helpful in understanding the problem and verifying the results from different experiments. This model is utilized as a reference to validate the vital signs experiments in different cases.

The organization of the thesis is as follow: Chapter two discusses the system development of the implemented SFCW system, chapter three shows the validation of the system for vital signs detection with the help of electromagnetic modeling, and chapter four shows the success of the system in fall detection with compressive sensing techniques while chapter five concludes the thesis.

CHAPTER TWO

SYSTEM DEVELOPMENT OF SFCW RADAR

This chapter illustrates the details of the implementation of a SFCW radar and also demonstrates our strategy to select an optimal operation frequency for the SFCW radar. The benefit of using SFCW radar system includes good range resolution, high signal-to-noise ratio, ability to discriminate targets in range, capability to reduce clutter within the resolution cell and its cost-effectiveness.
We will describe a single channel and multichannel SFCW radar block diagrams and will introduce miniaturization scheme of the conventional SFCW radar system to be portable integrated platform that we have developed through the course of this effort.

2.1 Design Consideration

The goal of this project to design and develop a SFCW radar with high range resolution. Some important design issues that have been considered include:

2.1.1 Signal Generation

The single channel SFCW radar system operates within 2 GHz to 4 GHz with 20 MHz frequency step size. The operating frequency waveform of the SFCW radar is linearly increased in discrete steps over the bandwidth in Figure 2.1. The frequency of the n^{th} pulse can be written as

$$f_n = f_o + N\Delta f \qquad (2\text{-}1)$$

where f_o is the initial carrier frequency, and Δf is the frequency step.

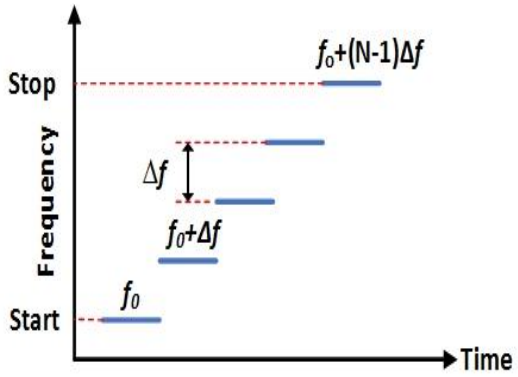


Figure 2.1. Step-frequency waveform generation in the time domain.

A stepped-frequency waveform achieves a wide bandwidth (NΔf) sequentially, but has a narrow instantaneous bandwidth of 1/τ where τ=1/Δf. The SFCW radar provides a high range resolution which is inversely proportional to its equivalent total bandwidth.

To generate the signal waveform, a direct digital synthesizer (DDS) is utilized for the SFCW radar. The IF signal is synthesized from the DDS board and the phase-locked loop (PLL) generates an RF stepped-frequency signal. For the multi-channel radar system implemented here, the center frequency of each DDS channel has been shifted by 1 GHz; while each channel covers 1 GHz. Hence, the total bandwidth of the stepped frequency signal is 2 GHz for a two-channel system. The frequency step and duration of each step are programmed as 20 MHz and 50 µs respectively, so that a 7.5-m unambiguous range (R_{un}) can be achieved using this equation

$$R_{un} = \frac{c}{2PRF} \tag{2-2}$$

Where PRF is pulse repetition frequency. The block diagram of the DDS board and PPL are shown in Figure 2.2. For more details about the signal generation readers are referred to [30].

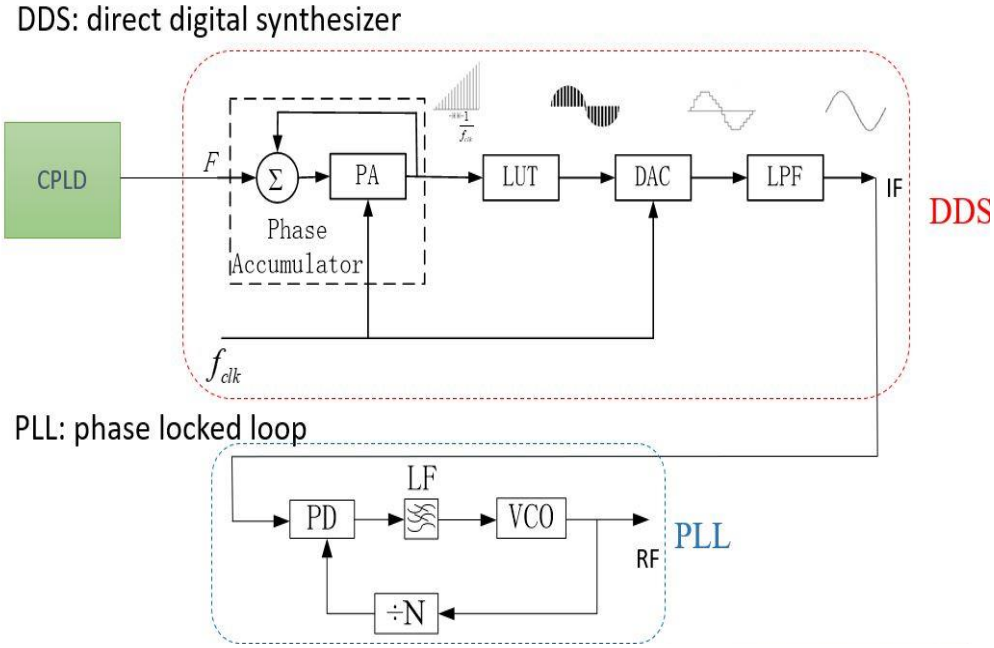


Figure 2.2. Signal Generator Based on DDS-Driven PLL Architecture.

2.1.2 Operating Frequency

At the preliminary stage, the functional goal of designing SFCW radar system is to simply detect vital signs of a human in a harsh environment such as rescue operation and military service. Therefore, the operation frequency of the radar system needs to be determined based on the function that the system is to accomplish. With this function in mind, the SFCW radar system is designed in the S-band range with a frequency band between 2 GHz to 4 GHz and a bandwidth of 2 GHz. The advantage of using higher-frequency transmissions to get wider bandwidth, hence higher range resolution but we must have low insertion loss to

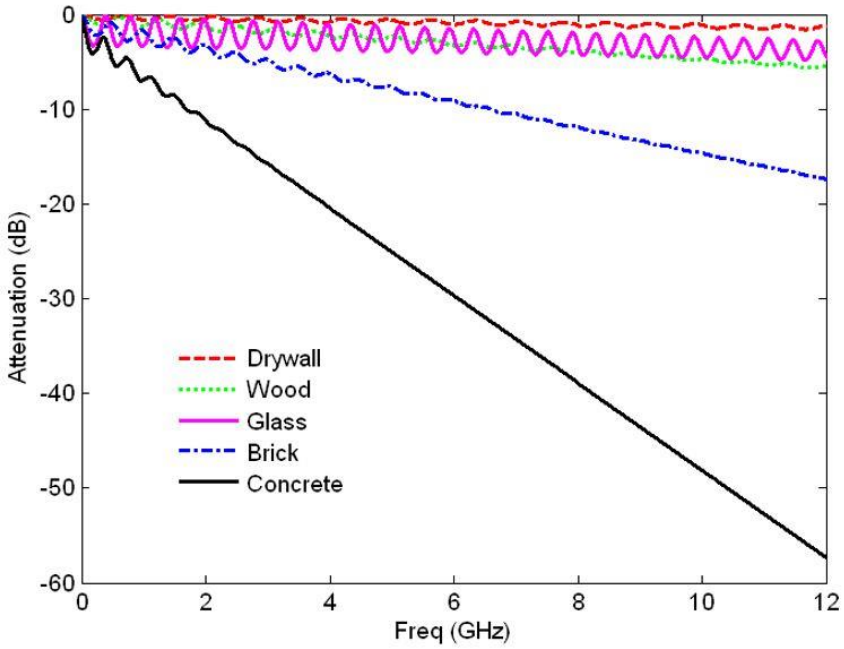


Figure 2.3. Simulated through wall reflection and transmission through various building materials.

Table 2.1. Dielectric Properties of Various Building Materials.

Material	**ε'**	**ε"**	**δ***
Concrete	6.8	0.9	0.13
Glass	6.4	0.032	0.005
Brick	4.0	0.2	0.05
Wood	2.5	0.05	0.02
Drywall	2.0	0.01	0.005

go through obstructing barriers. For the development of the SFCW radar system, there is need to be accounted the through barrier attenuation in many applications. It is well-known that through barrier attenuation increases with frequency. Hence, a lower frequency band usage is preferred to minimize the see-through insertion loss for high signal to noise ratio or even receive an adequate detectable signal after going a round trip propagation through the wall.

To better understand the through barrier attenuation of a SFCW radar signal, transmission characteristics are reviewed for various building materials. The propagation characteristics through the drywall, wooden wall, glass, brick wall, and concrete wall over the DC-12 GHz frequency range are presented in Figure 2.3 and Table 2.1.

It is very clear that loss due to drywall is typically low, but for concrete and cement walls it is relatively high at high frequency, however, it is acceptable still around 2 GHz, and could be used for our implementation.

2.2 Design Parameters

Normally, the stepped-frequency radar transmits a burst of N pulses, whose carrier frequencies are increased from pulse to pulse by a constant frequency increment Δf. Assuming the carrier frequency of the first pulse is f_0, the frequency of the nth pulse is then $f_n = f_0+(n-1)\Delta f$. The mathematical expression for a frame of the transmitted stepped-frequency signal (i.e. a burst) can be formulated as

$$s(t) = \frac{1}{\sqrt{T}} \sum_{n=0}^{N-1} \mathrm{rect}\left(\frac{t - nT}{T} \right) \exp\left[j2\pi \left(f_0 + n\Delta f \right) t \right] \tag{2-3}$$

where *rect(.)* is the rectangular function, T is the pulse repetition time (PRT), and the total time of a burst is $T_N = NT$. Assuming the instantaneous distance between the target and radar is $R(t)$, the received signal can be represented as

$$s_r(t) = as\left[t - 2R(t)/c \right] \tag{2-4}$$

where is the amplitude of the received signal, and c is the speed of light. The received signal is demodulated with its corresponding carrier frequency and then sampled in the baseband. The normalized sample of the baseband signal can be expressed as

$$s\left(f_n, m \right) = \exp\left[-j4\pi f_n R\left(m \right) / c \right] \tag{2-5}$$

where m represents the burst number. Here, we assume that the instantaneous range of the target does not change during the period of a burst, which is a

reasonable assumption given that the period of a burst is usually very short, e.g. several milliseconds and the displacement of the target during the period of a burst is less than a range resolution cell.

According to (2-5), we can acquire the high-resolution range profile (HRRP) of the target by performing an inverse fast Fourier transform (IFFT) along each burst. This procedure can be expressed as

$$\begin{aligned} x(k,m) &= \sum_{n=0}^{N-1} s\left(f_n, m\right) \exp\left(j2\pi nk / N\right) \\ &= \exp\left[-j\pi\left(N-1\right)\left(k_m - k\right)/N\right] \exp\left[-j4\pi f_0 R\left(m\right)/c\right] \\ &\cdot \frac{\sin\left[\pi\left(k_m - k\right)\right]}{\sin\left[\pi\left(k_m - k\right)/N\right]} \end{aligned} \tag{2-6}$$

where *k = 0, 1, …, N-1*, and $k_m = 2R(m)N\Delta f / c$. The first two terms represent the phase information of the HRRP, while the third term is the amplitude of the HRRP. When *k* is equal to k_m, the HRRP achieves its maximum and its position represents the range of the target, while the first term has little contribution to the phase as its value is nearly one. The second phase term also contains the range information of the target, which is highly ambiguous as the phase cannot be larger than 2π. However, based on the principle of differential interferometry, the displacement of the target during the period of a burst can be calculated as

$$\Delta R = \frac{4\pi}{\lambda} \angle\left[x\left(k_m, m+1\right) x^*\left(k_m, m\right)\right] \tag{2-7}$$

Where $(\cdot)^*$ denotes the complex conjugate, $\angle(\cdot)$ denotes the phase of the complex data, and λ is the wavelength of the signal.

The radar range equation provides an indication of the ability of the radar to detect the presence of a target. The equation is based on the Friis transmission equation and can be written for power received as a function of range for a given transmit power, wavelength, antenna gain, and radar cross section (RCS).

$$P_r = P_t G^2 \frac{\lambda^2}{(4\pi R)^2} \frac{\sigma}{4\pi R^2} \tag{2-8}$$

Where P_t is the transmitted power, *G* is the gain of the antenna, σ is the radar cross section RCS and *R* is the range. The transmitted output power is chosen to be 30dBm, because we needed penetration through barrier at a distance of 1-2 m in Table 2.2. We can use a power level as low as 8 dBm for normal vital signs detection where the distance is 1m from the subject.

In practice, the reflected signal is corrupted by thermal noise, interference and clutter. Therefore, it is essential to measure the minimum detectable signal P_m which depends on receiver bandwidth (*B*), noise figure (*F*), temperature (*T*), and required signal-to-noise ratio (*S/N*).

$$P_m = kTBF(S/N)_{min} \tag{2-9}$$

The available input thermal noise power is proportional to the product *kTB* where k is Boltzmann's constant, T is temperature (degrees Kelvin) and B is receiver noise bandwidth in hertz. The SFCW radar design parameters is shown in Table 2.2.

Table 2.2. System Design Parameters.

System Parameters	**Value**
Transmitter Output Power	30 dBm
Receiver Bandwidth	2 GHz
Receiver Thermal Noise Floor	(-174 dBm/Hz=-114 dBm/MHz) + $10\log_{10}(2000)$ -81 dBm
Center Frequency	3 GHz
Receiver Noise Figure	4 dB
Signal to Noise Ratio	6 dB
Receiver Sensitivity	Thermal noise floor+ Receiver NF+ S/N) = -71 dBm
1 dB compression point	12 dB
Receiver Dynamic Range	1 dB compression-Receiver sensitivity = 83 dB

2.3 System Description

Basically, the main three components of the SFCW radar system are the transmitter, receiver and antenna. It is essential to understand these three components.

2.3.1 Single Channel system

The block diagram of our single-channel SFCW radar system is shown in Figure 2.4. The DDS chip achieves an ultra-wideband of 1 GHz and uses a 1.2-GHz reference clock. The DDS channel synthesizes an IF signal with a bandwidth of 20 MHz, after which a 50 times PLL is used to acquire the RF stepped-frequency signal. The RF stepped-frequency signal is firstly divided into two components through a two-way power splitter. One component of is fed into a power amplifier before being sent for transmission through a horn antenna. The other component is split again with a quadrature hybrid coupler to serve as the in-phase and quadrature-phase local oscillator. On the receiver side, after a Hittite HMC753 wideband low noise amplifier (LNA), the received signal is split into its two constituent components and each is mixed with its corresponding local oscillator and unwanted components are filtered to acquire the baseband signal. Each baseband signal is then digitized and converted to a 14-bit digital signal and stored in a PC for further processing using a low speed data acquisition card. The implemented SFCW radar system is shown in Figure 2.5.

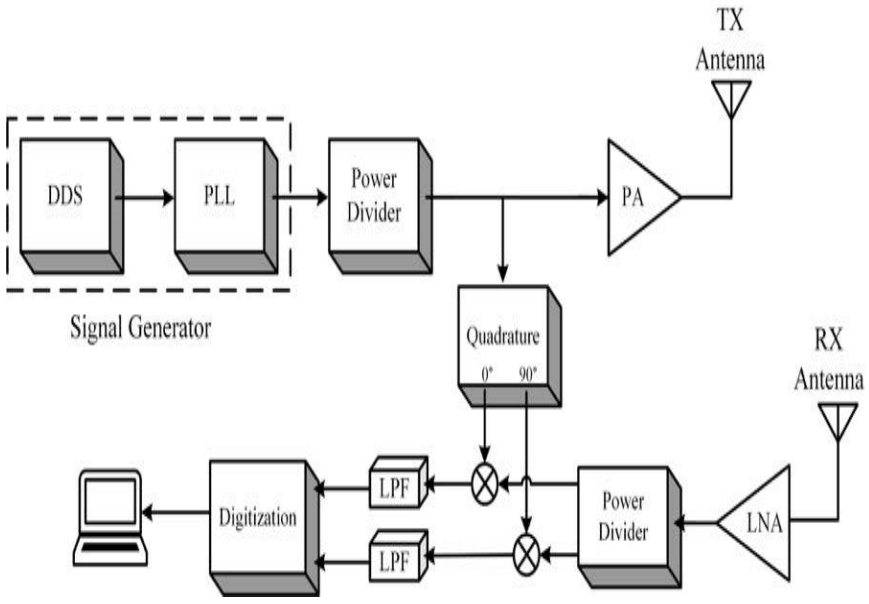


Figure 2.4. Top-level block diagram of the single channel SFCW radar system.

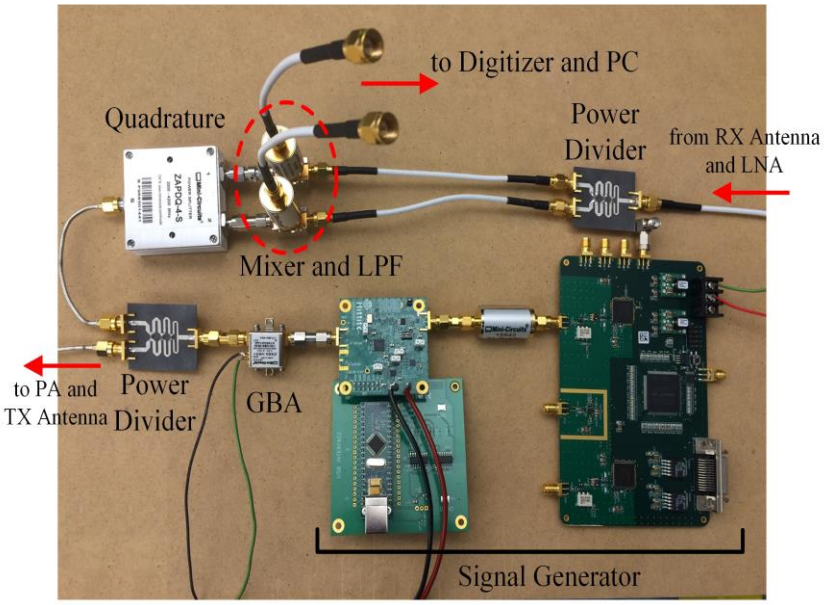


Figure 2.5. Single channel implemented system of SFCW radar.

2.3.2 Multi-channel system

The advantage of using a multi-channel stepped-frequency continuous wave radar is that it can achieve even wider bandwidth through dividing the spectrum into many channels, and all channels operate simultaneously, i.e. parallel processing. Our proposed two-channel SFCW radar system is shown in Figure 2.6. Each DDS board has two DDS channels integrated on a single platform and work simultaneously to achieve the whole ultra-wide bandwidth. The two boards are synchronized using one 1.2-GHz reference clock (master). Even though we have ultra-wide band for the whole system, it is still relatively easy to use low speed analog to-digital converters due to the very low instantaneous bandwidth.

In the design of two channel SFCW radar, the transmitter is designed in a way that it transmits adequate peak power at the desired frequency bandwidth, which is determined by the required radar range. The primary components of the transmitter of the two channel SFCW radar are waveform generator (DDS & PLL), gain block amplifier, attenuator, power divider and power amplifier. Four channel SFCW radar system is illustrated in Figure 2.7.

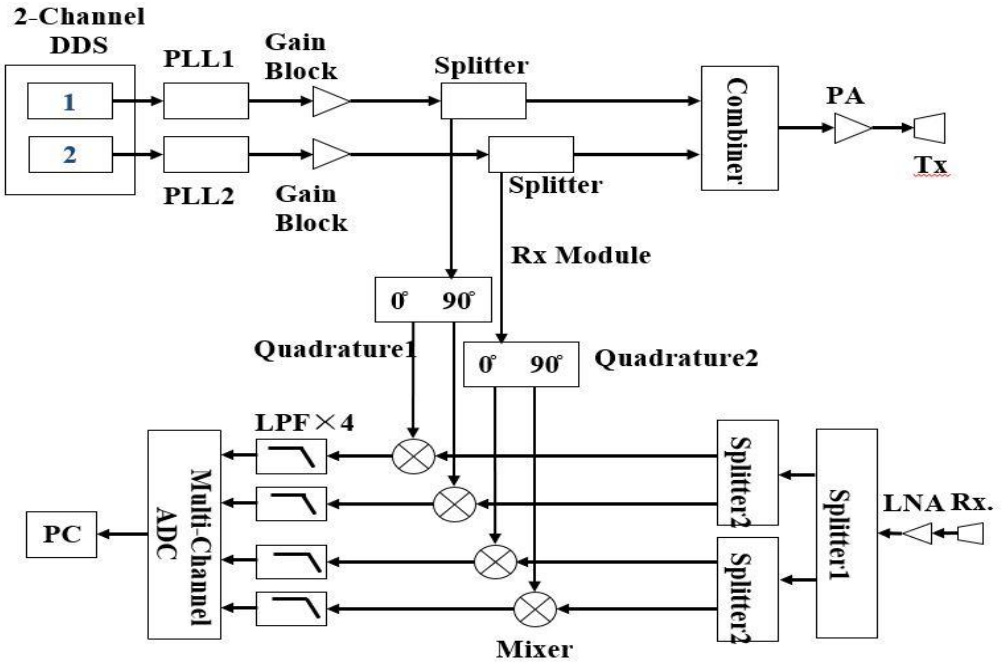


Figure 2.6. Block diagram of two channel SFCW radar.

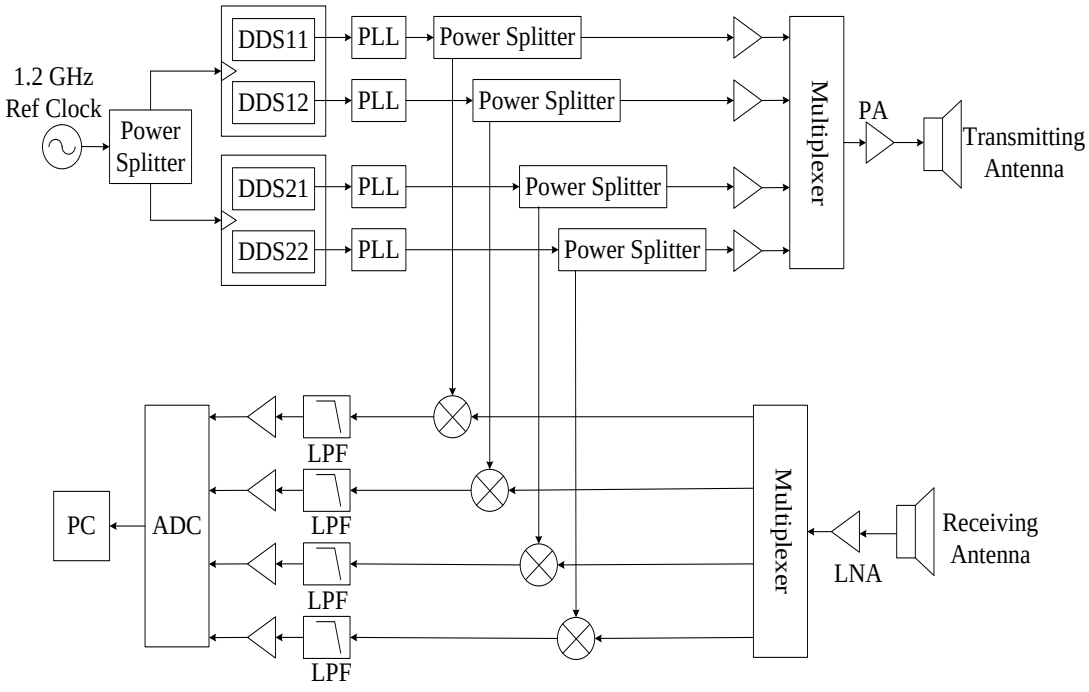


Figure 2.7. Block diagram of four channel SFCW radar.

2.3.3 Link Budget Analysis of Two Channel System

Figure 2.8 shows the link budget of the transmitter of the two channel SFCW system with a summary of the associated power levels. The stepped frequency signal is generated from DDS and PLL. The Mini-Circuits ZX60-V63+ Gain Block is used with a +19.2dB gain at 3 GHz, with an acceptable return loss better than 10 dB. The Mini Circuits ZVE-8G+ power amplifier is utilized before transmitting antenna. The output 1 dB compression point of the power amplifier is +30 dBm.

At the receiving side, there are four main components: mixer, quadrature hybrid 'Q-hybrid', LNA and filters. The detailed link budget of the receiver is outlined in Figure 2.9. In this radar system design, the Mini-Circuits QSC-722+ Q-hybrid provided a phase-shifted carrier of 0º and 90º to the mixers. The Q-hybrid has better than 15dB return loss, less than ±0.5dB amplitude imbalance and an error of less than 3º between ports, signals to be mixed with the received signals after amplification. As the received signal is captured by another horn antenna and is amplified by a Low Noise Amplifier (LNA). Afterwards it is divided into two parts for the I-Q mixer. Mini-Circuits ZX05-C-60+ mixer to mix the LO with the RF received signal, and it is used since it has 32 dB of isolation from LO to RF ports from 2 GHz to 4GHz and low conversion loss. After the down-conversion by the mixer, there is a need to filter unwanted components from the baseband signal. Therefore, a low pass filter is added after down-conversion. The Mini-Circuits SLP-1.9+ low pass filter is inserted in the RF front-end. Finally, the baseband signal is digitized using a low-speed data acquisition card and stored in a personal computer for subsequent processing.

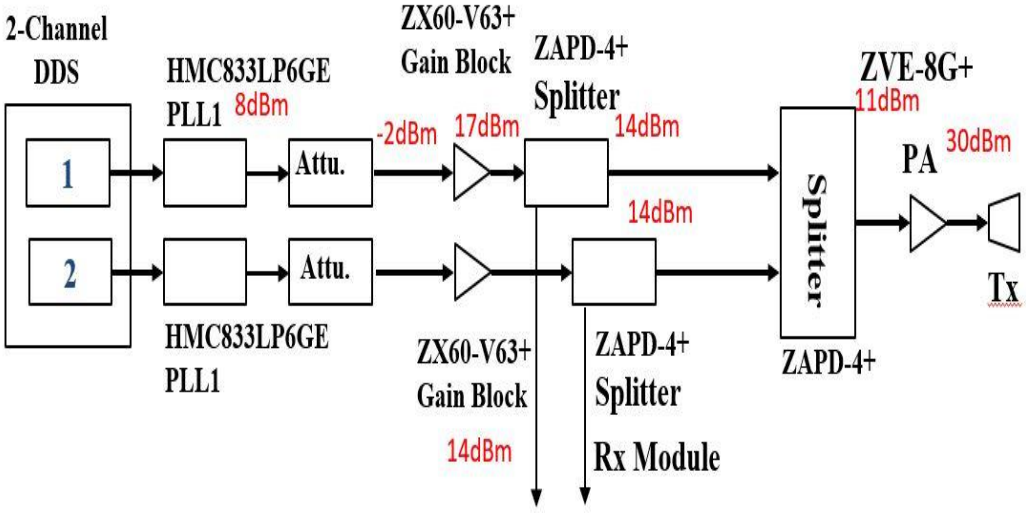


Figure 2.8. Link Budget analysis of transmitter.

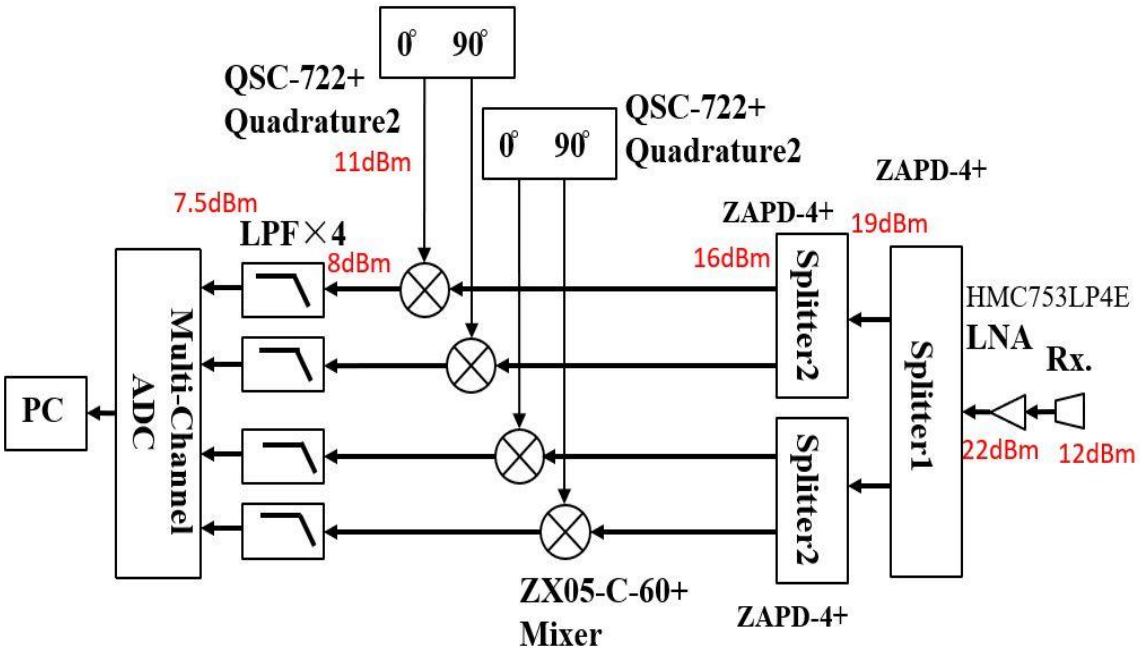


Figure 2.9. Link Budget analysis of receiver.

2.3.4 Compact proposed radar system

This section describes the development of a new compact module with improved performance, with significant size and power reduction over the original prototype.

The main design goals of the SFCW radar system design are the preservation of a small size factor and a small weight to be portable. Therefore, the system is designed in printed circuit board with respective ICs to reduce the size of the integrated prototype. The 3D view of PCB stack-up configuration of the SFCW radar system is shown in Figure 2.10.

For minimizing the interference of the integrated system, the whole system design is divided into five different boards in Figure 2.11 and the interconnections among the different boards is done using flexible coaxial cable.

The transmitter of SFCW radar is integrated on FR4 boards and Rogers 4350 laminate. The board is separately stacked up for avoiding EMI problem. Figure 2.12 illustrates the fabrication of the transmitter board. The components used for the integrated boards are listed in Table 2.3.

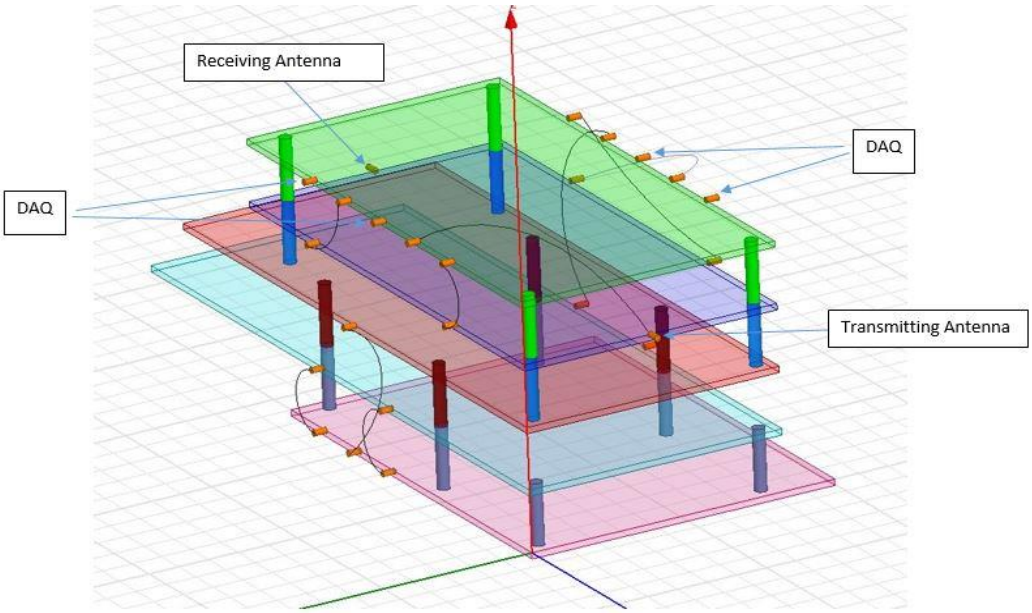


Figure 2.10. Stack-up SFCW radar system.

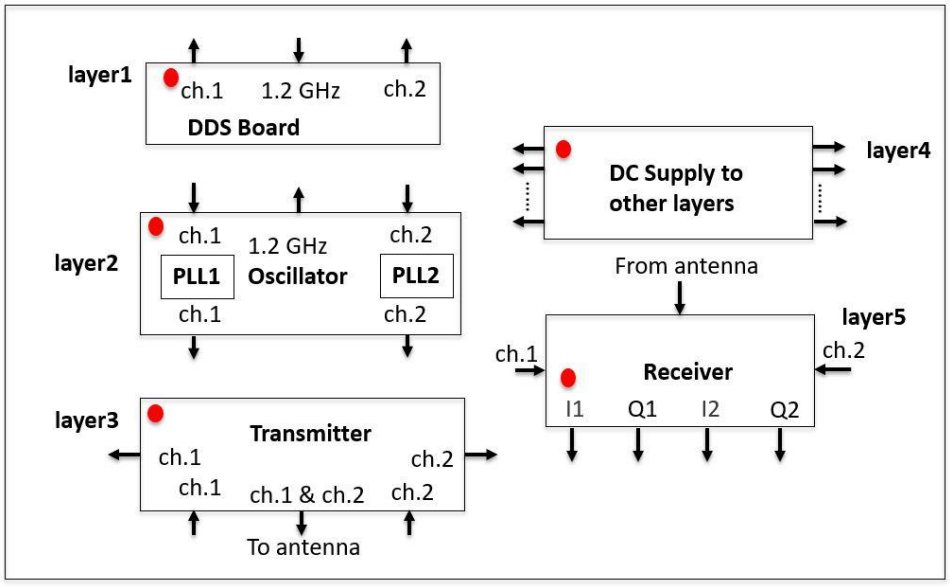


Figure 2.11. SFCW Radar Stack-up Implementation.

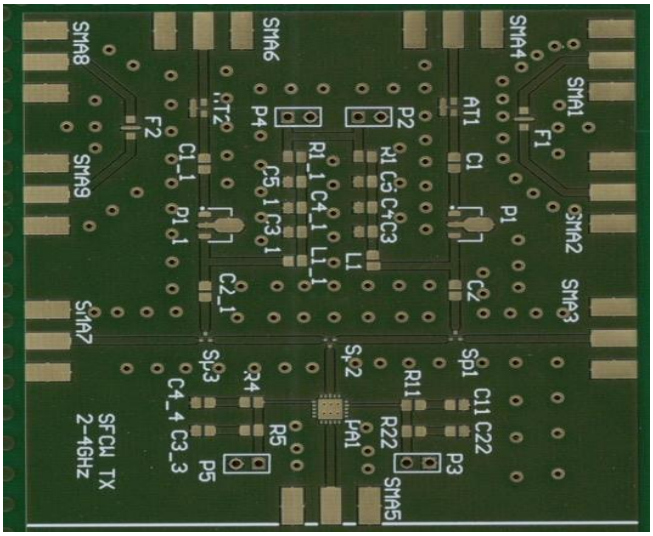


Figure 2.12. The fabricated FR4 board of the transmitter.

Table 2.3. Components used in integrated transmitter.

Symbols in Block Diagram	Chips	Description
Gain Block	Hittite, HMC589LP3	21 dB gain, DC-4 GHz, 5V supply
Splitter/Combiner	Susumu, PS1608GT2-R50-T5	2 Way-0° 0 to 20 GHz
PA	Triquint, TGA2597-SM	25V, -27.5V, 2-6 GHz

The receiver board is fabricated on FR4 and Rogers 4350 laminate. The respective integrated chips are listed in Table 2.4. The layout of the receiver board is shown in Figure 2.13.

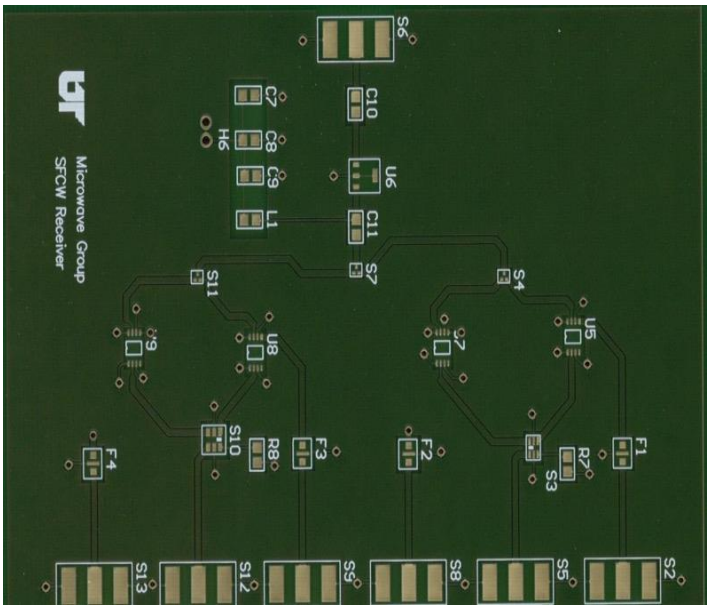


Figure 2.13. The fabricated board of the receiver.

Table 2.4. Components used in integrated receiver.

Symbols in Block Diagram	Chips	Description
LNA	HMC639	0.2-4GHz, NF 2.3 dB, Gain 13 dB
Splitter1/Splitter2	Susumu, PS1608GT2-R50-T5	2 Way-0° 0 to 20 GHz
Mixer	Hittite, HMC175MS8E	8 dB conversion loss, LO/RF 1.7-4.5 GHz, IF DC-1 GHz
Quadrature1	Mini-circuits, QCS-332	2 Way-90° 1800to 3300 MHz
Quadrature2	Mini-circuits, QCS-442	2 Way-90° 2800to 4400 MHz
LPF	TDK, MEM2012F10R0	DC-10 MHz

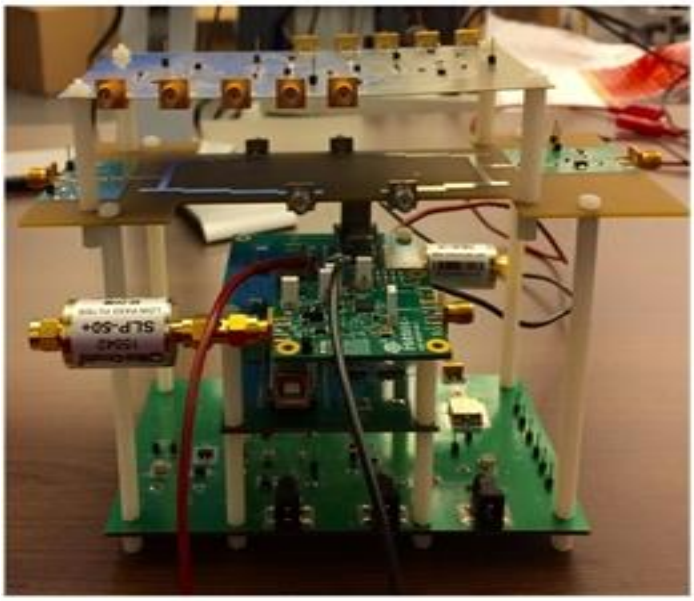


Figure 2.14. Stack-up implementation of two-channel SFCW radar system.

Figure 2.14 illustrates an overview of the stack-up system. The prototype is implemented using five boards for DDS, the transmitter, the receiver, the oscillator and the power supply. The Transmitter, Receiver and Power Supply PCB's are separated by blank single-sided FR4 PCB's. These blank grounded copper clad boards provided adequate isolation between the individual power supply, transmitter and receiver boards. The SFCW radar prototype is successfully implemented and the performance of the prototype is similar to the conventional system.

2.4 Conclusion

In this chapter, single channel, multi-channel and finally a compact SFCW radar system is designed and implemented, which can transmit a set of frequencies simultaneously via one UWB antenna over multiple channels operating in parallel. In many applications, a hand-held radar system is desired for simultaneous monitoring of accurate vital signs detection and localization capabilities. The performance of the SFCW radar system will be evaluated and the applicability of this SFCW UWB radar system, e.g., precise target localization, fall detection and vital signs detection will be investigated.

CHAPTER THREE[1]

AN ELECTROMAGNETIC MODEL OF HUMAN VITAL SIGNS DETECTION AND ITS EXPERIMENTAL VALIDATION

In this chapter, Non-contact vital signs detection using a stepped-frequency continuous wave radar is presented. To validate the experimental results, an electromagnetic model using the scattered fields of incident plane waves on a dielectric model of a human subject has been developed. The model approximates the torso by an equivalent homogenous dielectric layer. The SFCW radar system results are accurate for both heart rate and respiration rate detection within 5% error margin when compared to conventional contact sensor readings. The agreement between measured and simulated results is acceptable for distances up to 3 m, and at various subject orientations with respect to the radar boresight. Meanwhile, in the presence of more than one subject, only slight drop in accuracy has been observed unless one subject is almost blocked by another. This system can be utilized to investigate various human activities and motion-scenarios as well, to validate the performance of radar system.

3.1 Background

There is a growing need to fully monitor and understand the different kinematics of human vital signs for many applications; such as monitoring elderly, and for aiding them with falling incidents, or discriminating between different daily human activities like walking, limping or running (e.g. gait analysis). Electromagnetic (EM) modeling of such scenes can help in developing and testing new design and detection concepts in early stages of system development. For instance, through the use of accurate EM modeling, one can study different rescue scenarios in natural disasters like earthquakes and landslides events and aid the development of effective radar systems to save lives. Numerous modeling methods have been already investigated for fast and accurate computations of scattered fields for various subjects using techniques such as ray tracing and EM numerical techniques [31-33]. In this work, we focus on modeling the human torso, which is the area that should be affected the most by respiratory and heartbeat motions. The torso is represented by a dielectric elliptical cylinder, and the chest and heart motions are emulated by expanding and shrinking the corresponding surface. Widely used radar systems for such applications are continuous wave (CW), ultra-wideband (UWB), frequency modulated continuous wave (FMCW) and stepped

[1] This chapter is a collaborative effort with Mr. Tuan Phan from The Catholic University of America, Mr. Farhan Quaiyum, Dr. Lingyun Ren from University of Tennessee and Dr. Ozlem Kilic from The Catholic University of America.

Table 3.1. Comparison between different radar technologies.

	CW	**UWB**	**FMCW**	**SFCW**
Localization	No	Yes	Yes	Yes
Multiple Subjects	No	Yes	Yes	Yes
ADC Speed	Low	Fast	Low	Low
Calibration	-	-	Difficult if nonlinearity exists*	Easy

frequency continuous wave (SFCW) systems. Different features of these systems are listed in Table 3.1. In this paper, we utilize a SFCW radar system; and are able to switch between its two operating modes: heart and breathing rates using CW for a single subject, while SFCW operation for locating heart and breathing rates and range of multiple subject(s) as well [11].

3.2 Electromagnetic Model

In this section, the human vital signs model is briefly described. The model developed by the Catholic University of America (CUA) assumes that the human torso, represented by a homogenous dielectric object is illuminated by a plane wave emanating from a stepped frequency radar source over 1 GHz bandwidth. The frequency range is uniformly sampled by a set of K frequencies f_k; ranging from f_1 to f_K with a frequency step size Δf. The signals are transmitted for each time frame with $\Delta T = 0.0469$ s; and subsequently the resulting scattered fields from the scene are calculated. The full-wave MLFMA model is run on a GPGPU cluster at CUA to calculate the scattered fields with significant acceleration. Since the scattered field is a function of both frequency and time, it is represented by a full matrix for all specified frequencies and time steps.

To represent the human subject more accurately, we improved our previously developed human subject model by utilizing a dielectric model rather than a perfect electric conducting boundary conditions [34]. Thus, we need detailed information on the material properties, as well as the shape of the human torso. Given that at the high frequency end of the operation frequency; i.e. 3 GHz, the lateral and anterior-posterior rib cage diameters of the torso correspond to 1.5 λ– 2.5 λ in free

space, the size of the problem would be relatively large. Model details and MLFMA process are discussed in the following sections.

The human torso is represented by an elliptical cylinder, which mimics the internal anterior-posterior rib cage diameters. The anterior-posterior, lateral rib cage diameter and diaphragm height corresponding to those dimensions are provided in Table 3.2 [35]. A local region on the top-left corner of this elliptical cylinder is periodically perturbed to simulate the periodic displacements on the chest wall due to heartbeat as shown in Figure 3.1. Meanwhile, the chest's anterior and lateral diameters expand and shrink periodically in both directions as a result of respiration [36]. The periodic chest wall and local region movements due to heartbeat can be approximated as sinusoidal models given by:

$$d_h(t) = d_{h,0} + m_h \sin(2\pi f_h t) \tag{3-1}$$

$$d_{ap/l}(t) = d_{ap/l,0} + m_{ap/l} \sin(2\pi f_b t) \tag{3-2}$$

where m_h, $m_{ap/l}$, are the heart and anterior-posterior/lateral and displacements amplitudes, $d_{h,0}$ and $d_{ap/l,0}$ are the heart and chest nominal diameters, respectively; and f_h, *and* f_b, are the heart rate and respiratory rate respectively.

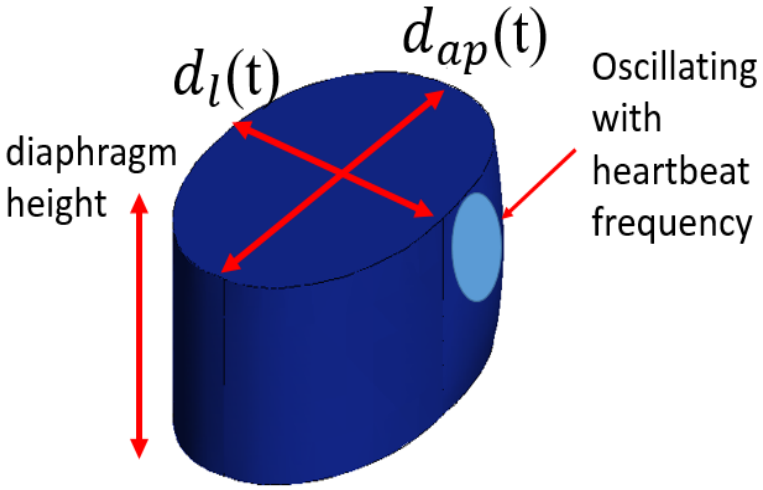


Figure 3.1. Human Torso Model Geometry.

Table 3.2. Simulated torso dimensions in normal respiration.

	Anterior-posterior diameter	Lateral diameter	Diaphragm dome diameter
Min.	15.2 cm	24.3 cm	20.6 cm
Max.	17.6 cm	25.6 cm	20.6 cm

The human torso is developed as an inhomogeneous medium comprised of different layers with different dielectric properties (e.g. skin, blood, bone, etc.); which are modeled as a multilayered structure in Figure 3.2 (a), [37]. We follow this step by creating an equivalent homogenous model for the torso that has the same transmission and reflection coefficients in the direction of interest for our experiments, as shown in Figure 3.2 (b) for the elliptical cylinder model described earlier in Figure 3.1. Rather than solving this complex problem, the calculations were simplified by using an equivalent single dielectric slab to replace the multilayer structure. The single slab has the same size and a homogeneous equivalent dielectric constant; maintaining that both structures have the same transmission and reflection coefficients over the entire frequency range of interest and for the direction of interest. The equivalent dielectric constant was calculated via a particle swarm optimization algorithm (PSO) [38]. This technique is inspired by the collective intelligence and social behavior of the bees searching for food.

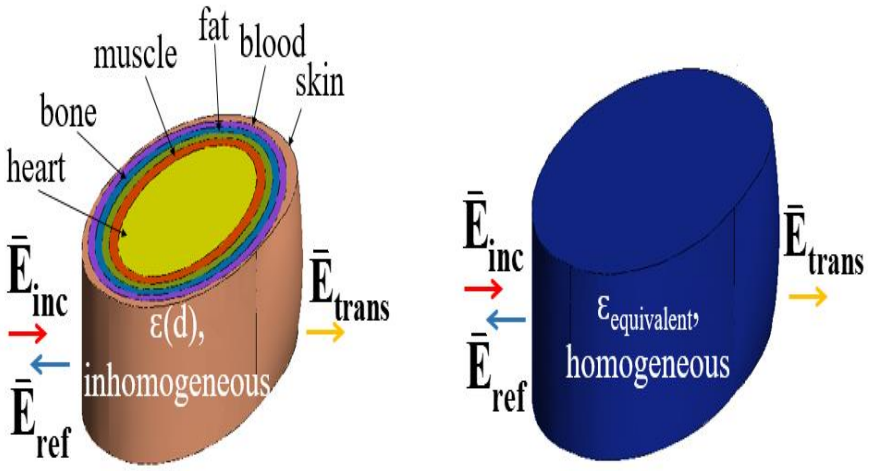


Figure 3.2. (a) Inhomogeneous medium of different dielectric layers. (b) Equivalent homogenous model.

At first, 25 agents (bees) are randomly distributed to sample the search domain; which is a two-dimensional space corresponding to the real and imaginary parts of the dielectric constant. We set the range from 1 to 100, and from -50 to 0, for the real and imaginary parts respectively. The fitness function for this application is the reflection coefficient, which is computed for each agent based on its location in the search space. Using the collective intelligence on each individual's best location, as well as a global best location that has been achieved by the swarm, each agent updates its velocity and location toward these best locations. The algorithm repeats itself until the desired convergence criterion is met (i.e. either the reflection coefficient error is less than 1% or the maximum number of iterations reaches 1000 in this case). More details about the PSO implementation can be found in [39].

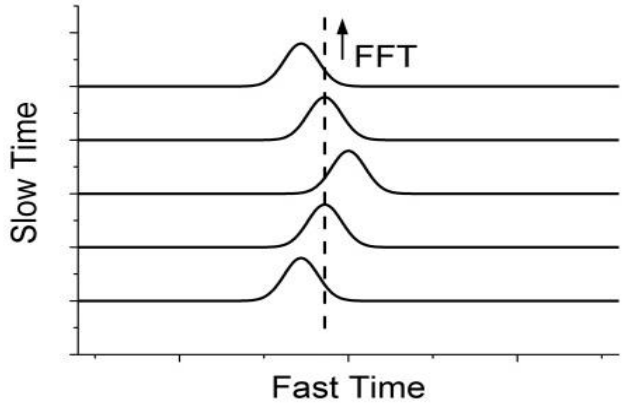
The material properties of each layer in the multilayer representation, and the optimization results for an equivalent homogenous representation are shown in Table 3.3 over a 4 GHz bandwidth. More information can be found in A.2, which is done by the Catholic University of America.

Table 3.3. Thickness, dielectric constant information of human body parts at different frequencies and their corresponding effective dielectric constant [37].

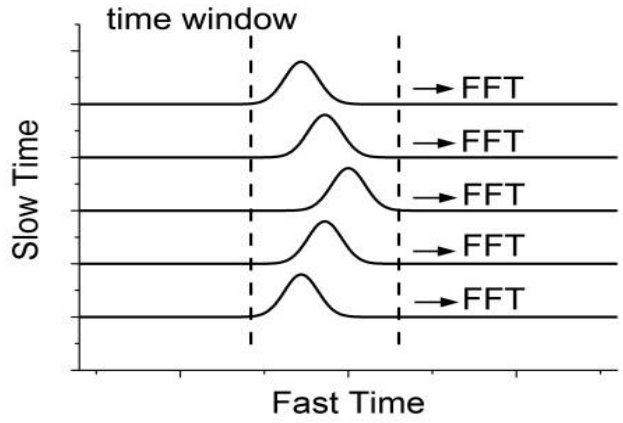
Frequency	**1GHz**	**2GHz**	**3GHz**	**4GHz**	**5GHz**
Skin 2mm	35.8-10.5j	35.05-7.9j	34.4-8.2j	33.7-9j	32.9-10.1j
Blood 1mm	58.7-21.4j	58.1-14.5j	57.5-13.8j	56.7-14.5j	55.7-15.8j
Fat 8mm	5-0.9j	4.8-0.7j	4.7-0.8j	4.5-0.8j	4.4-0.9j
Muscle 10mm	54.1-12.2j	53.3-11.1j	52.3-12.5j	50.9-14.6j	49.3-16.6j
Bone 10mm	8.5-0.8j	7.9-1.2j	7.5-1.3j	7.2-1.3j	7.0-1.7j
Heart 60mm	60.3-19.3j	59.3-14.9j	58.2-15.6j	56.7-17.3j	55.1-19.4j
Effective Dielectric Constant (91mm)	21.45-12.0j	21.9-12.1j	22.5-12.3j	23.2-12.6j	24.1-13.27j

3.3 Phase based Methods

In the conventional approach, the frequency of displacements modulating the collected sample amplitudes can be identified by applying the direct FFT method to slow-time samples. As presented in Figure 3.3 (a), phase-based methods first implement FFT on each pulse along slow time for direct phase variation extraction.



(a)



(b)

Figure 3.3. (a) Conventional FFT method to detect vital signs (b) Proposed phase-based methods.

Alternatively here, in order to extract the vital signs information, we apply a phase-based method on the received baseband signal [40,41]. As presented in Figure 3.3 (b), phase-based methods first implement FFT on each pulse along slow time

for direct phase variation extraction. The harmonic and intermodulation interference of respiration are suppressed using the phase information because of the linear relationship between phase and time delay. FFT is performed next on the fast time samples [42],

$$\begin{aligned} Y(t,\nu) &= \left[A_p P(\nu) \exp\left(-j2\pi\nu\tau_d(t)\right)\right] * \delta(\nu+\nu_c) \\ &= A_p P(\nu+\nu_c) \exp\left[-j2\pi(\nu+\nu_c)\tau_d(t)\right] \end{aligned} \tag{3-3}$$

where * represents convolution. For the FFT of each pulse, the computation complexity is minimal at dc compared with any other frequency. As a result, FFT of each pulse at dc is

$$\begin{aligned} Y(t,0) &= \sum_k \left[I(t,\tau_k) - jQ(t,\tau_k)\right] \\ &= A_p P(\nu_c) \exp\left[-j2\pi\nu_c\tau_d(t)\right] \end{aligned} \tag{3-4}$$

It is worthwhile mentioning that synchronization between FPGA clock and carrier frequencies helps in eliminating the jitter in the system for the proposed phase-based method. Suppose the jitter in the FPGA clock is $J(t)$, then the signal of interest at the receiver will be

$$r'(t,\tau) = A_p p\left(\tau - \tau_d(t) - J(t)\right) \tag{3-5}$$

When the system clock and carrier frequencies are synchronized, there will be phase coherence between these two frequencies, i.e., the two different frequencies are phase locked. The intermediate signals of *I*/*Q* channels and collected pulses are

$$I(t,\tau) = r'(t,\tau)\cdot\cos\left(2\pi\nu_c\left(\tau - J(t)\right)\right) \tag{3-6}$$

$$Q(t,\tau) = r'(t,\tau)\cdot\sin\left(2\pi\nu_c\left(\tau - J(t)\right)\right) \tag{3-7}$$

$$\begin{aligned} y(t,\tau) &= I(t,\tau) - jQ(t,\tau) \\ &= r'(t,\tau)\cdot\exp\left(-j2\pi\nu_c\left(\tau - J(t)\right)\right) \end{aligned} \tag{3-8}$$

When FFT is applied on the fast time samples of (16), we obtain

$$
\begin{aligned}
Y(t,\nu) &= \left[A_p P(\nu) \exp\left(-j2\pi\nu\tau_d(t) - j2\pi\nu J(t)\right)\right] \\
&\quad * \left[\delta(\nu+\nu_c)\exp\left(j2\pi\nu_c J(t)\right)\right] \\
&= A_p P(\nu+\nu_c)\exp\left[-j2\pi(\nu+\nu_c)\tau_d(t)\right] \\
&\quad \cdot \exp\left(-j2\pi\nu J(t)\right)
\end{aligned}
\tag{3-9}
$$

When each pulse is Fourier transformed at dc, (3-9) will become (3-5). In this manner, the jitter existing in the FPGA clock can be eliminated from the demodulated phase information using proposed phase-based methods.

As summarized in Figure 3.4, in the phase-based method, FFT is applied on each pulse first within a time window and along “fast” time, then direct phase variation extraction is implemented. A time Hamming window was utilized, and its optimized length is three times that of the frequency samples.

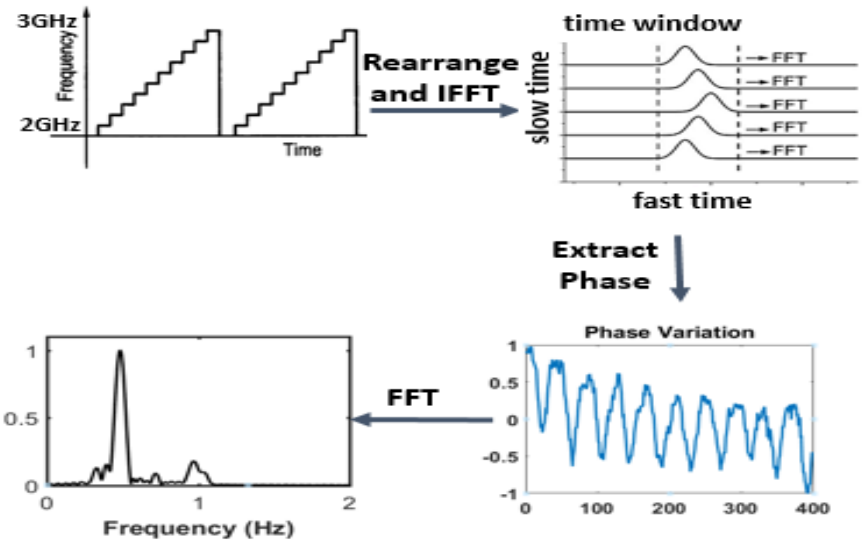


Figure 3.4. Steps of phase-based method to detect vital signs.

Phase based methods use the phase and time delay linear relationship, which drastically suppresses both harmonic distortion and intermodulation products in the retrieved phase information. The retrieved signal has two terms: one is the summation of the frequency components and the second is a dc term. The dc term is mainly a result of the imbalance between the I and Q channels, and we use mean subtraction here to remove both baseband dc and dc offset. By extracting

and analyzing the phase of the fast-time samples along a traversed range bin of a subject as shown in Figure 3.4, the displacements caused by respiration and heartbeat can be readily calculated by arctangent demodulation method [43], or complex signal demodulation [43], or state space method [44] or combination.

3.4 Experimental Validation

In this chapter, for experimental validation, four different scenarios were investigated: (a) a single subject was positioned at different orientations with respect to the radar, (b) a single subject was positioned at different distances from the radar, (c) a single subject lying down, (d) two subjects present in the scene. The utilized radar has a transmitted power of 8 dBm, uses two 9 dB gain horn antennas, and its receiver sensitivity is -71 dBm. The phase-based method has been applied to measured data to extract the heart rate and respiratory rate similar to the steps used in simulation [40, 41].

The normal respiration rate of an adult at rest is 12 to 20 breaths per minute, while heartbeat is 60 to 80 beats per minute. Hence, for a person with the slowest breathing rate (i.e. 12 breaths/min) and heartbeat (60 beats/min), 15 second is about 5 cycles of breathing and 15 cycles of heartbeats. These many cycles, would be enough to extract the information of motion. Furthermore, we also want to minimize the corresponding simulation computational time for our modeling efforts for comparison. Thus, in this paper we have considered 15 seconds as an appropriate amount of time needed to run the measurements. Definitely, fewer cycles can be used. For instance, fewer cycles can be employed for detection, and we can keep updating the rates by using say 2 cycles at a time (moving average), to allow faster real time displays.

The observation time; i.e. 15 seconds corresponds to 320 slow-time samples that were acquired. During the experiments, a commercial pulse sensor and respiratory contact sensor were also used to record the heartbeat and respiration rates of the subject(s) and are used as the ground truth. The measured and simulated deviations (errors) from these contact sensor readings are quantized by:

$$\text{Error} = \frac{Ps - Pm}{Ps} * 100\% \tag{3-10}$$

where P_s is the commercial contact sensor result and P_m is either the measured or simulated result.

3.4.1 Subject at different orientations

In the first experiment, the subject position was fixed at 1 m away from the radar [24]. The subject had a height of 165 cm, waist size of 78 cm, and was sitting on a

chair with the main beam of the antennas in line with her torso level. Four different orientations with respect to the radar were considered as shown in Figure 3.5.

Simulated and measured results are shown in Figure 3.6 for these four cases, while Table 3.4 shows the heart and respiratory rates recorded by the contact sensors for the four cases and compares them to both the simulated and measured results. The respiratory frequency errors are within 4%, and heart rate errors are within 2.5%, for both simulations and measurements as listed in Table 3.4 Generally, smaller radar cross-section (RCS) or further distance from the heart leads to an increased error. As expected, the reference case is the best among the four scenarios investigated for simulations, as it has the largest RCS.

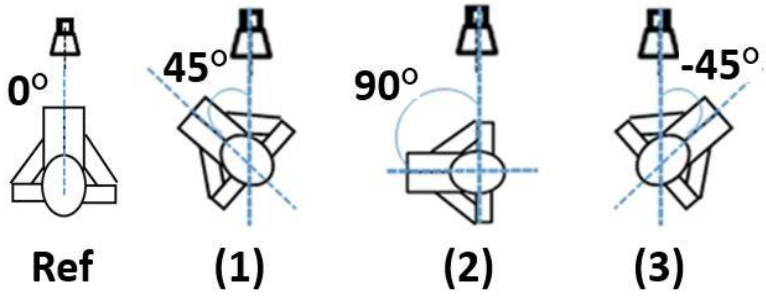


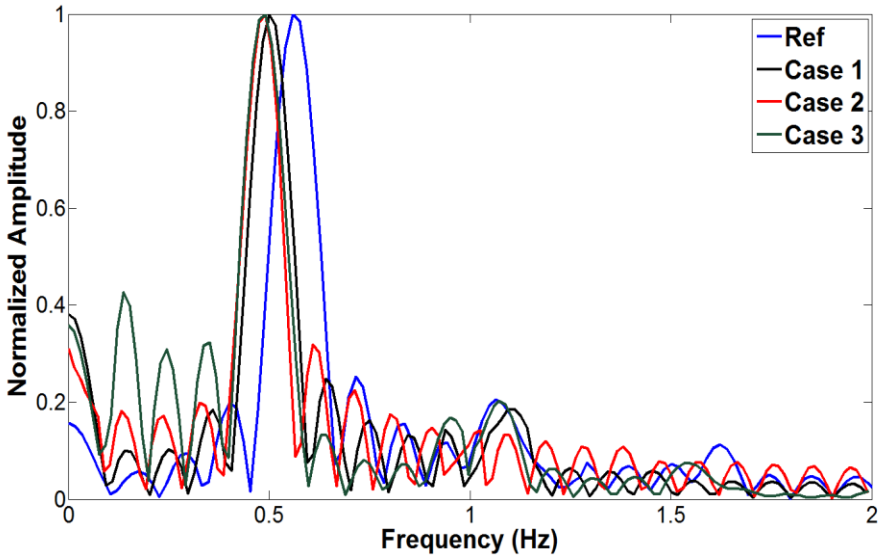
Figure 3.5. Subject at different angles. Ref 00, (1) 45°, (2) 90°, (3) -45°.

Table 3.4. The respiratory rates and heart rates from the contact sensors and simulated and measured radar results for the four different orientations.

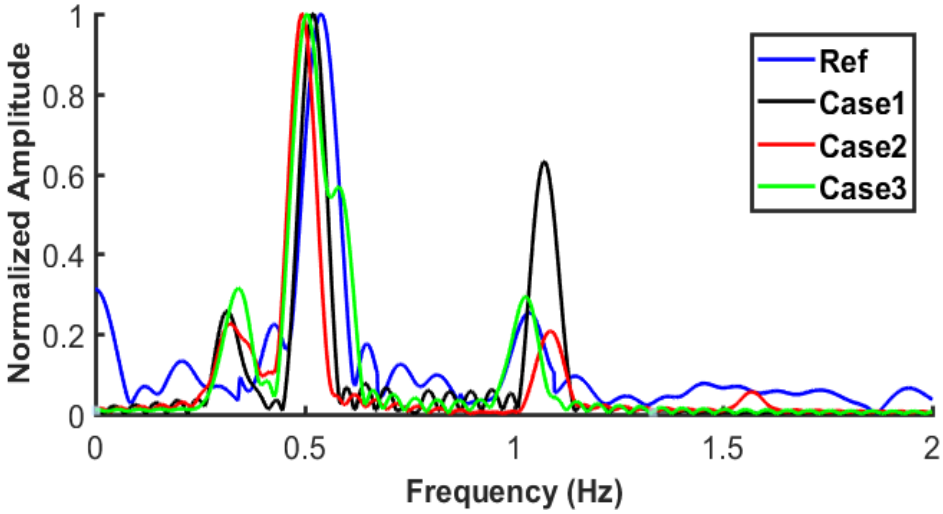
Case	Sensor RR(Hz)	Simulated RR (error)	Measured RR (error)	Sensor HR(Hz)	Simulated HR (error)	Measured HR (error)
Ref.	0.558	(0.14%)	(2.20%)	1.043	(0.47%)	(0.67%)
1	0.510	(1.57%)	(2.52%)	1.101	(0.99%)	(2.26%)
2	0.475	(3.78%)	(2.85%)	1.091	(2.44%)	(1.60%)
3	0.499	(0.16%)	(1.70%)	1.063	(0.94%)	(1.89%)

Similarly, simulation results show that case 3 results are the least accurate for both respiratory rate and heart rate due to the lower RCS, and the relative position of the heart, which is on the farther side with respect to the radar. However,

experimentally it is difficult to see such distinct differences for various practical reasons in the measurement setup, yet such effects still result in less than 3% error.



(a)



(b)

Figure 3.6. The breathing rate and heart beat based on: (a) simulated data (b) measurement for subject in different orientations.

3.4.2 Subject at different distances

In the second experiment, the same subject was positioned in front of the radar with the normal to the torso aligned at 0° degree with the radar boresight. The subject was placed at 1 m away laterally from the radar at first, then was subsequently moved to 3 m away as shown in Figure 3.7 and the results are shown in Figure 3.8. The errors for the heart and respiration rate detection of these different cases are shown in Table 3.5 Both simulation and measurement results show that the error worsens as the subject gets further away. As expected, the further the subject is the weaker the received power.

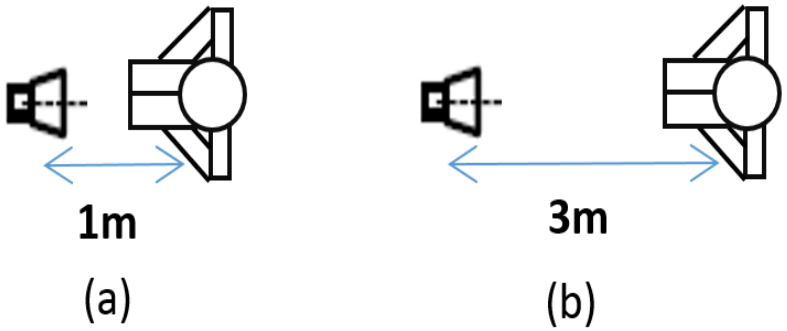


Figure 3.7. Subject at different distances (a) 1m, (b) 3m.

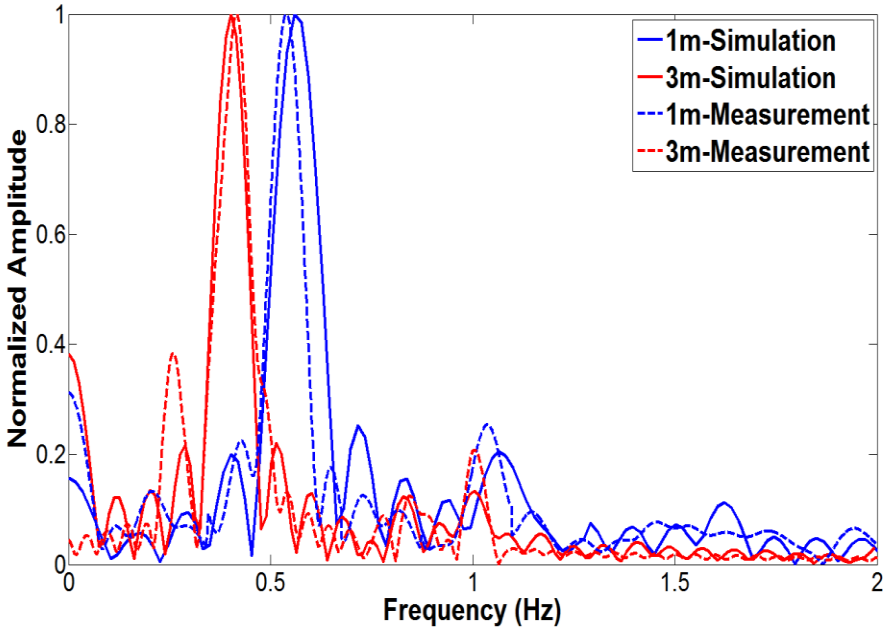


Figure 3.8. The breathing rate and heart beat based on simulated and measured data.

Table 3.5. Error percentages for different distances.

Case	Sensor RR(Hz)	Simulated RR(error)	Measured RR(error)	Sensor HR(Hz)	Simulated HR(error)	Measured HR(error)
1 m	0.558	(0.14%)	(2.20%)	1.043	(0.47%)	(0.67%)
3m	0.40	(2.25%)	(3.50%)	1.045	(2.85%)	(4.30%)

3.4.3 Subject lying down on ground

In the third experiment, we investigated the case when the same subject is lying down on the ground. The antenna is pointing down to the subject at an oblique angle as shown in Figure 3.9.

The sensor readings for breathing rate and heart beat are 0.45Hz and 1.120Hz, respectively. Although there is a ground effect in this scenario, both simulation and measurement are pretty close to the sensor readings due to the relatively large RCS. The errors for respiration and heartbeat are 0.22% and 0.53% respectively for simulation, while the measurements are at 2.22% and 1.34%. The results are plotted in Figure 3.10. Table 3.6 shows simulated and measured HR and RR for the subject lying down.

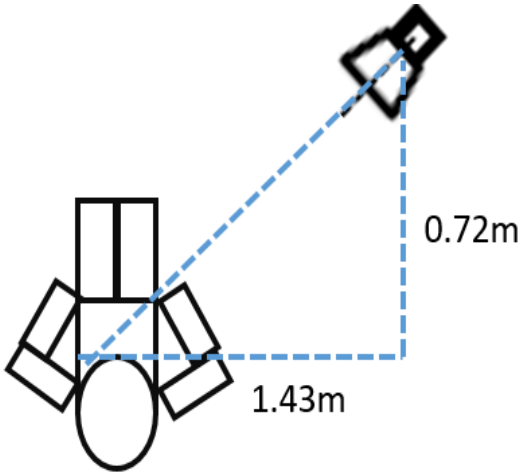


Figure 3.9. Person under test is lying on ground.

Table 3.6. Error percentage for detecting vital signs for a lying down subject.

Sensor RR (Hz)	Simulated RR (error)	Measured RR (error)	Sensor HR (Hz)	Simulated HR (error)	Measured HR (error)
0.450	(0.22%)	(2.22%)	1.120	(0.534%)	(1.34%)

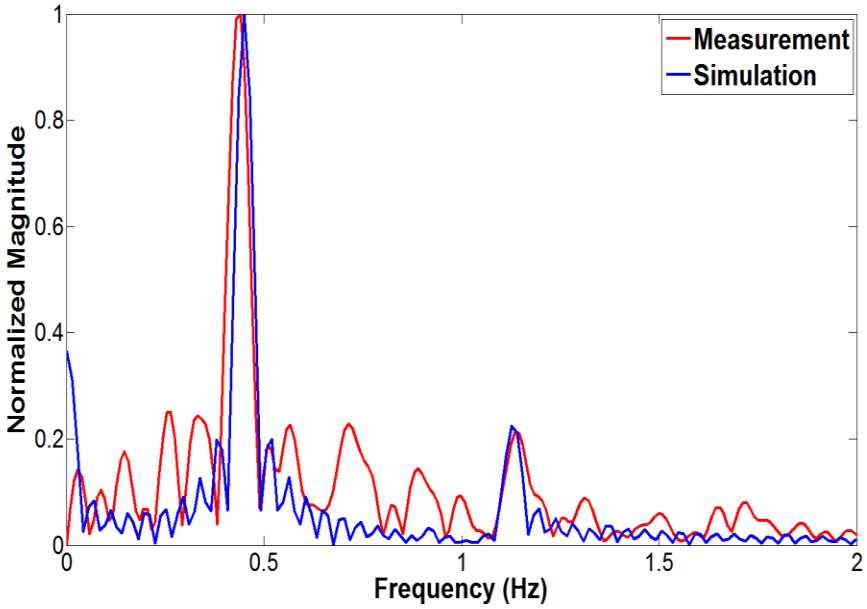


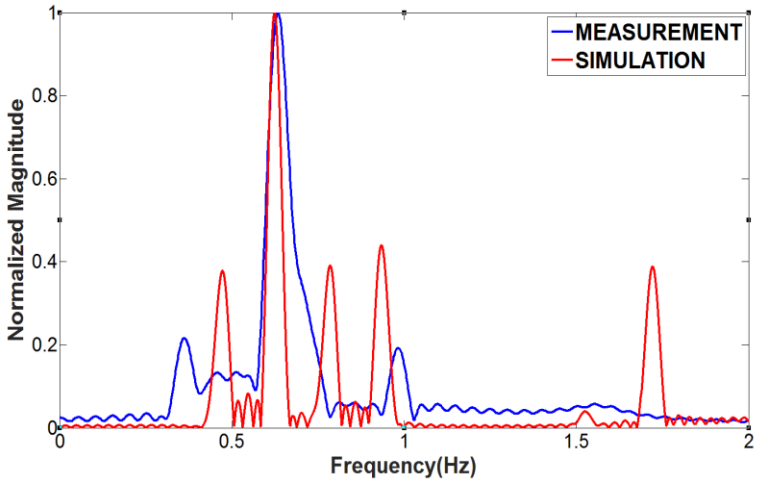
Figure 3.10. Simulation and measurement results for person under test lying on the ground.

3.4.4 Multiple subjects in the scene

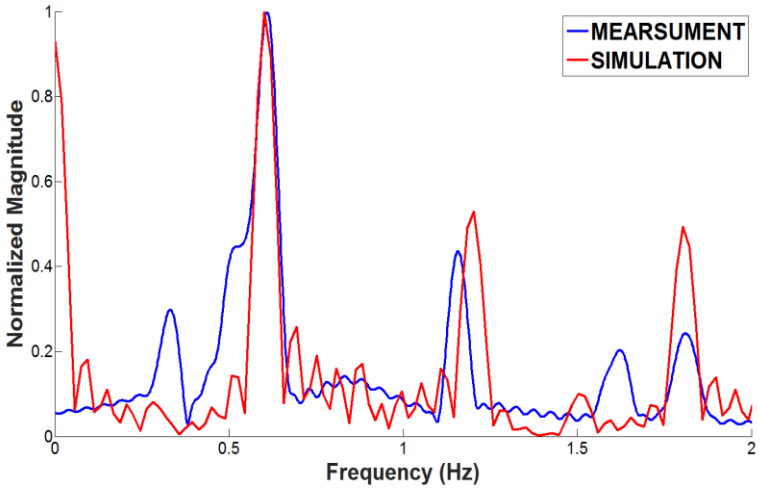
In the fourth experiment, we simultaneously detect the vital signs of two persons [45]. We performed two sets of experiments to investigate the effect of the physical spacing between those two subjects on detecting their vital sign accuracy as a function of their transversal and longitudinal spacing. First, we placed the two subjects sitting down at different lateral distances, and symmetrically off-centered with respect to the radar boresight direction; with a distance d_y between the two subjects in the transverse direction as depicted in Figure 3.12. We acquired both simulation and measurements results. Figure 3.11 (a) and (b) show the respiratory frequencies and heartbeats of the two subjects at d_y=0.6 m and indicate good agreement between measured and simulated results for both subjects.

Table 3.7. Error percentage for detecting vital signs for two subjects.

Sub.	Sensor RR (Hz)	Simulated RR (error)	Measured RR (error)	Sensor HR (Hz)	Simulated HR (error)	Measured HR (error)
1	0.62	(1.61%)	(1.61%)	1.2	(0%)	(3.33%)
2	0.61	(0.16%)	(1.23%)	0.98	(3.06%)	(1.02%)



(a)



(b)

Figure 3.11. The vital sings spectrum showing respiration and heart rate for (a) 1st person. (b) 2nd person.

The detected heart rates and breathing rates utilizing the contact sensors, and the relative error of the simulated and measured errors are shown in Table 3.7. It appears that the discrepancy between simulated and experimental data is slightly higher compared to the case when only one subject is in the scene, but errors (deviations) are still within 3.5%.

3.4.5 Effect of transversal distance between subjects

In this experiment, one subject was sitting down at a fixed location (0.9 m, -0.5 m) away from the radar; i.e. slightly off boresight direction (Figure 3.12) such that the first subject was within the main beam of the antennas. The second subject is at coordinates (1.6 m, 0.5 m), i.e. the two subjects were initially spaced by d_y=1 m in the lateral direction. The second subject kept stepping closer to the first subject in the lateral direction such that their lateral separation d_y changed from 1 m to 0.2 m in steps of 0.2 m. As expected, we were able to estimate the respiration rate clearly when the subjects were farther away, but the measurement errors were slightly increased as the second subject started to get closer to the first subject and started to be blocked gradually.

When the second subject was at 0.2 m away from the first, the error exceeded 5%, as the second subject was almost completely blocked by the first one. The simulation results show the error rate varies from 0.24% to 3.73% for 1 m and 0.2 m separations, respectively. Table 3.8. lists the measured respiration rate using both the sensor and radar and their associated percentage errors. Figure 3.13 shows clearly the received vital sign signals when the spacing is relatively large (making them distinctly recognized), and when the two subjects are in close proximity and the signal then is highly corrupted (noisy).

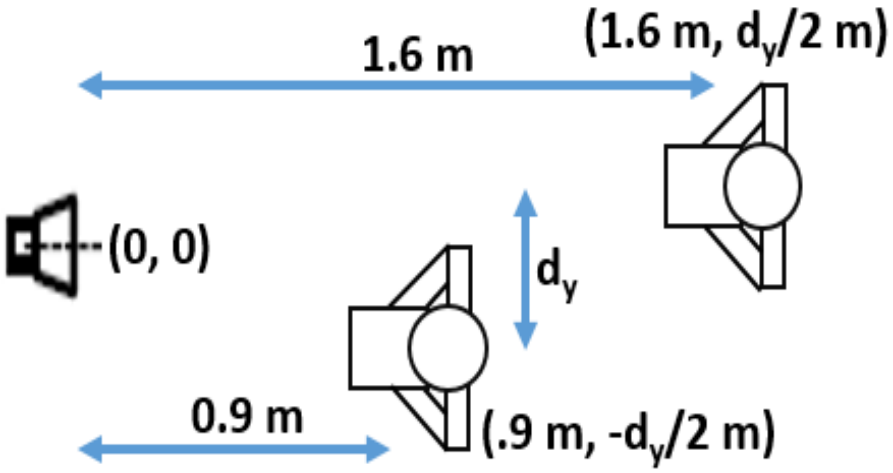


Figure 3.12. Setup of two human beings under test where the transversal distance between them is variable.

Table 3.8. Error percentage for detecting respiration for two subjects with different transversal distances.

Distance d_y (m)	Sensor (Hz)	Radar (Hz)	Error Rate (%)
1.00	0.401	0.402	0.25
0.80	0.4762	0.4799	0.78%
0.60	0.4386	0.444	1.23%
0.40	0.4261	0.4394	3.12%
0.20	0.5013	0.4698	6.3%

3.4.6 Effect of longitudinal distance between subjects

In this experiment, one subject was sitting at (0.9 m, -0.3 m) away from the radar and the second subject (while also in a seated position (initially at (1.5 m, 0.3 m)) started getting gradually closer to the radar, with d_x varying from 1.5 m to 1.0 m. as depicted in Figure 3.14. The transversal distance between the two subjects was maintained constant at 0.6 m. Again, we were able to clearly detect the respiration rate of the two subjects when they were further apart. But when the spacing between the two subjects was less than the range resolution of the radar, the vital signs between the two subjects overlapped, and the respiration could not be distinctively identified. Table 3.9 shows the increase in the respiration rate detection error as the distance between the subjects is decreased.

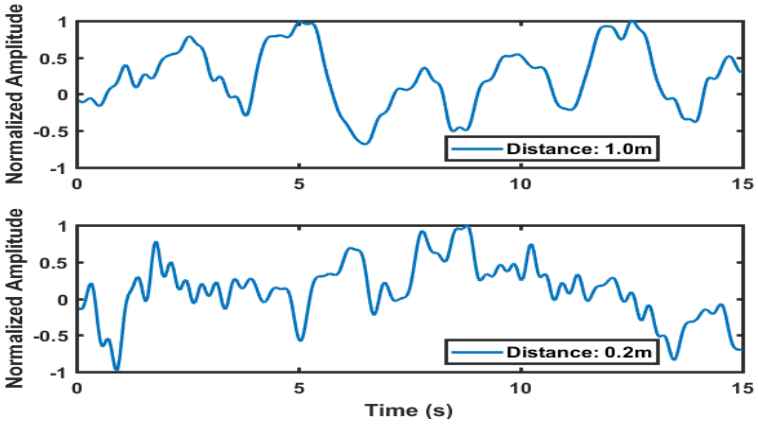


Figure 3.13. Extracted time domain respiration signal from radar data for two distances showing the effect of spacing between the two subjects.

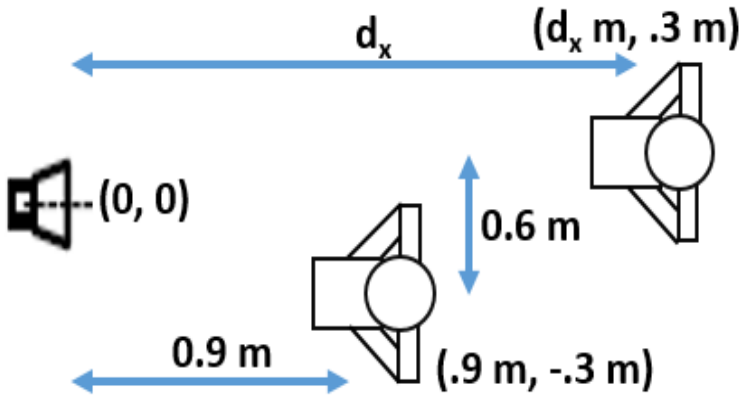


Figure 3.14: Setup of two human beings under test where the transversal distance between the subjects are varied.

Table 3.9. Error percentage for detecting respiration for two subjects with different longitudinal distances.

Distance d (m)	Sensor (Hz)	Radar (Hz)	Error Rate (%)
1.5	0.477	0.479	0.42
1.3	0.520	0.510	1.90
1.1	0.420	0.433	3.10
1.0	0.503	-	-

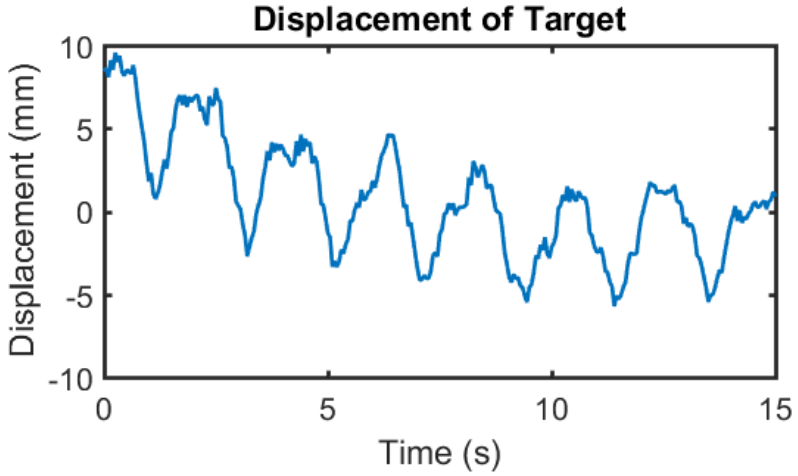


Figure 3.15. Detection of displacement due to vital signs detected by radar.

3.5 Discussion

The developed SFCW radar can detect chest displacement as indicated in Figure 3.15, and as demonstrated above both heart rate and respiration rate can be detected even in a noisy environment. Table 3.10 shows a comparison of our developed radar with state-of-the-art research. The detection error of vital signs is comparable with other reported work. In [31], error rates less than 1% was achieved with the use of special dc offset cancellation technique. The results show that the detection accuracy of the SFCW radar performance is around 3% when the subject is facing the radar and up to 1 m away and conventional FFT signal processing was used to extract these rates. Due to low signal to noise ratio (SNR) the error rate is relatively high. To further enhance the accuracy of the respiration and heart rates detection, the state-space method (SSM) can be used. SSM is a parameter estimation algorithm with robustness against noise and efficiency in computation [32]. These detection techniques reduce the impact of the interfering harmonic signals, thus improving the SNR of the detected vital sign signals. In [22], we utilized the phase information of acquired signals and combined SSM method with either complex signal demodulation (CSD) or arctangent demodulation (AD) techniques and achieved higher accuracy < 1.5%.

3.6 Conclusion

We intend to benefit from developing a highly accurate EM model for scenes that include various human activities; so we can fine-tune our signal processing and hardware development in designing a proper radar system for human activity monitoring and detection. The developed EM model for heart rate and respiration rate detection accuracy has been validated and it approximates the torso by a homogenous equivalent dielectric layer, while utilizing an accelerated parallel version of the multi-level fast multipole algorithm to speed up the computation.

To validate the human vital signs EM model, a SFCW radar operating over 1 GHz bandwidth has been developed. SFCW radars are typically relatively easy to build and calibrate but newer generations of FMCW radars have been recently introduced and have addressed many of their known shortcomings like non-linearity and could even outperform SFCW performance and will be considered in our future studies. Meanwhile, the results shown by our current model of the SFCW radar performance is accurate (the error rate is around 3%); when the subject is facing the radar and up to 1 m away. However, when the subject is farther away or at different angles facing the radar or there are multiple subjects in the scene, the performance could be slightly degraded due to reduced RCS or lower signal to noise ratios, and subsequently error goes up to 6%. The presence of more than one subject and in close proximity definitely causes pronounced interference and signal distortion.

Table 3.10. Comparison of the proposed SFCW Radar performance with other state-of-the-art research.

Research Group	Radar	Operating Frequency	d	TX Power	Error %	Application	Signal Processing
This work	SFCW	2-3 GHz	1m	8 dBm	<3	Vital Sign Detection, Multiple person tracking	FFT
M. Li et al. [32] 2018	CW	5.8 GHz	-	-	3.5	Fast Heart Rate Detection	Wavelet-transform based data length variation technique
Peng et al. [33] 2017	FMCW + CW	5.64-5.96 GHz	1.5m	8 dbm	-	Localization, ISAR Imaging, Vital Sign Detection	-
L. Qiu et al. [34] 2017	SFCW	2.15–2.75 GHz	3.5m	20 dBm	-	Through wall life signal extraction	Isophase based signal extraction
Ren et al. [22] 2016	Impulse	1.5-4.5 GHz	0.8m	-28 dBm	1.5	Vital Sign Detection	SSM-AD
Huang et al. [26] 2016	CW	2.4-2.5 GHz	1m	-10 dBm	<3	Vital Sign Detection	Upper-bound and linear matrix inequality relaxation
Wang et al. [27] 2015	FMCW	75-85 GHz	1m	-3 dBm	8	Vital Sign Detection	FFT
Chioukh et al. [28] 2014	Harmonic CW	12 & 24 GHz	0.5m	10 dBm	<4.4	Vital Sign Detection	-
Vinci et al. [29] 2013	CW	24 GHz	1m	-5.6 dBm	-	Vital Sign Detection	FFT
Lazaro et al. [11] 2010	Pulse	3.1-10.6 GHz	1m	-	≤2.4	Vital Sign Detection	Moving target indicator canceller
Park et al. [30] 2007	CW	2.4 GHz	1m	8.3 dBm	<1	Vital Sign Detection	AD

The developed model has proven to be accurate and can be extended to analyze various human activities including walking, fall events and eventually to other human activities including gait analysis for better understanding of motion kinematics.

CHAPTER FOUR[2]

ALTERNATIVES TO BIG DATA ACQUISTION USING STEP FREQUENCY CONTINUOUS WAVE RADAR AND COMPRESSIVE SENSING ALGORITHMS

Various methods to continuously track elderly in an indoor environment have already been successfully developed. However, these methods are data intensive and require handling and storing of massive data. Here, we target developing efficient methods to reduce the amount of acquired data to speed the detection process, and we demonstrate here their potential in the context of fall detection. A combination of hardware and software solutions is needed to achieve this objective. For that purpose, we utilize stepped-frequency continuous wave radar (SFCW), which does not require a continuous frequency spectrum like the impulse UWB or even the FM radars. Use of SFCW simplifies the implementation of compressive sensing (CS). CS can be used to reduce the size of the acquired data to significantly below the Nyquist threshold. In our demonstration, we use phase information contained in the obtained complex high-resolution range profile (HRRP) to derive the motion characteristics of the human subject, including the instantaneous velocity, acceleration and jerk. The obtained data is utilized for non-contact fall detection and healthcare monitoring. The effectiveness of the proposed method is validated using measured results.

4.1 Background

There is a trend to develop methods to handle BIG data, which will have great impact on our problem's solving capabilities that require massive storage and data streaming. For the time being, it is essential to develop alternatives based on smart data handling. This strategy requires developing a combination of elegant hardware and sophisticated software tools. As an example, in health care industry, there is a need for a 24/7 tracking of elderly people in indoor environments. Luckly, wireless technology has recently emerged as a key for health monitoring by providing benefits in terms of convenience and accuracy in diagnosis, treatment, and detection of emergency situations in home and clinical environments. Specifically, this technology could be even more significant for elderly people for whom injuries sustained from fall incidents at home are considered the most dangerous cause of fatal accidents. Instant detection of fall events significantly

[2] This chapter is a collaborative effort with Mr. Nghia Tran from The Catholic University of America, Dr. Lingyun Ren from University of Tennessee and Dr. Ozlem Kilic from The Catholic University of America.

lowers the mortality risk of the elderly people, which in turn enhances the feasibility of their independent living. This process using the current methods; such as FM or impulse UWB radars, would generate massive data, and would require unrealizable storage capabilities. Alternatively, the use of stepped frequency continuous wave radars (SFCW) can considerably reduce the amount of acquired data, given that SFCW radars are based on the discretization of the spectrum rather than using a continuous spectrum like in FM or impulse UWB radars. Additionally, to drastically reduce the volume of acquired data, we apply compressive sensing algorithms and could utilize levels in the range of 10%. To illustrate our effort, we present our work here on monitoring and tracking of fall incidents of an elderly person in his or her home, but the work could be extended for monitoring other activities as well.

Fall detection, in particular, is considered to be a major public health problem, as a fall would usually result in a serious disability for the elderly. Studies show that rapid detection of a fall event and immediate assistance after a fall can greatly reduce the adverse effects on the elderly [46]. Therefore, it is of great importance to develop a way to detect a fall automatically by using non-contact methods, and to report the fall incident to the related medical personnel so that proper care can be provided immediately. But, typically this would require keeping large amount of data records almost on a 24/7 basis and would even become impractical if we need to simultaneously track multiple people.

Many methods have been developed for fall detection in recent years [47]. There are basically two different categories for fall detection: wearable devices and non-wearable devices. The simplest detection method for wearable devices is based on a necklace or wristwatch with a button, which can be manually activated in a fall case. The wearable devices are inexpensive and easy to set up. However, they still carry some potential risk, as they cannot be activated in the event of a loss of consciousness after a fall, and the person may not wear them all the time. In this chapter, we focus on the non-wearable devices, which are non-contact, and usually involve multiple installed sensors to acquire the data when a person is in close proximity to these sensors. Table I lists the current available non-contact systems and their disadvantages.

Due to the drawbacks of these aforementioned fall detection technologies, there is a need for more practical solutions. The sought-off solutions that target fall detection and based on narrow band radar techniques have been investigated by many researchers and even though numerous promising results have been already been demonstrated, but they have still some drawbacks. For example, the radar prototypes developed in [51-53] are all narrowband Doppler radars; and work at a single tone using the Doppler principle to estimate the relative velocity of the target within a given detection range. But, a human fall is comprised of a series of

Table 4.1. Various methods of non-contact fall detection and their disadvantage.

Method	Disadvantage
Floor Vibration Sensor [48]	Difficulty in detection in presence of other objects
Acoustic Sensor [49]	Difficulty in detection in presence of other objects
Camera Based Device [50]	Privacy problem
Doppler Radar [51-53]	No range information of the targets

human body part movements, and even though the fall incident can be recognized based on its Doppler signature measured by one frequency, but, these narrowband Doppler radars have no ability to provide the range information of the target, so the extracted Doppler signature will be distorted if there is more than one moving target in the scene.

On the other hand, SFCW radar method has emerged as a promising solution due to its high signal-to-noise ratio, sensitivity and less stringent hardware requirements. The waveform of this SFCW radar system can be configured to work either as a single tone or as a SFCW mode allowing multi-functionality as well [54]. Ref [53] for example has utilized SFCW radar for fall detection. It is very effective in detecting fall events and in simultaneously localizing and tracking more than one person.

In this chapter, we introduce our developed SFCW radar system for fall detection and also apply our compressive sampling algorithm that relies on the sparsity of the acquired signal. Presence of sparsity of the signal acquired to be accurately reconstructed with significantly fewer samples than the required by Nyquist-rate sampling [55]. The utilized data acquisition algorithm (Orthogonal Matching Pursuit: OMP) is designed to detect human fall utilizing the SFCW radar collected data based on a random selection of the measurement frequencies. The OMP algorithm used here significantly reduces the data acquisition time while reducing the amount of data to be processed compared to the conventional processing method.

4.2 Compressive Sensing Algorithm

Generally, let **x** denote a desired signal of N samples, which can be represented in an orthonormal basis Ψ ($N \times N$) in terms of $\mathbf{x}=\Psi\mathbf{s}$ where **s** is the $N \times 1$ column vector of weighting coefficients. The signal **x** is K-sparse; that is, all but K of its entries are zero. In the spirit of CS, instead of recording the N entries in **x** directly, we record a smaller number M ($K < M << N$) of linear measurements of **x**. Since these measurements are linear, we can represent the measurement vector **y** as

$$y = \Phi x = \Phi\Psi s = \Theta s \tag{4-1}$$

where the measurement vector y is an $M \times 1$ vector, Φ is an $M \times N$ measurement matrix. We define the sampling matrix (or projection matrix, mapping matrix, or dictionary) $\Theta = \Phi\Psi$ with a size of $M \times N$. The measurement matrix Φ must allow the reconstruction of the length-N signal x from $M<<N$ measurements, since this problem generally appears ill-conditioned with $M < N$. However, if the measurement matrix Φ and the orthonormal basis Ψ are mutually incoherent, this problem becomes well-conditioned [123]. Typically, Φ is designed in the form of randomized characteristics. In many cases, it is common to select Φ as a binary matrix containing a single randomly positioned 1 in each row, while Ψ is chosen as a $N \times N$ discrete Fourier transform (DFT) matrix. It is worth noting that the measurement process is not adaptive, meaning it is fixed and does not depend on the signal x. CS allows the recovery of a K-sparse signal x from M ($\approx K$) measurements with high probability. The CS reconstruction problem is formulated as an optimization problem as follows:

$$\hat{\mathbf{s}} = \min \|\mathbf{s}\|_1, \text{ such that } y = \Phi\Psi s' = \Theta s' \tag{4-2}$$

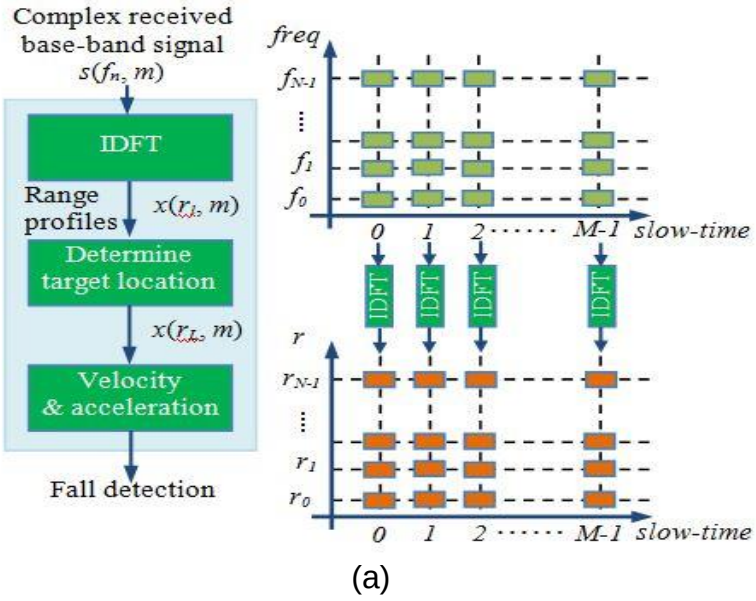
For further details of the fundamental principles of CS theory is presented in A.3.
In order to implement the CS reconstruction algorithm. The relationship between the received baseband signals $s(f_n,m)$ and the range profile $x(r_l,m)$ can be expressed as a Fourier transform as follows:

$$s(f_n, m) = \sum_{l=0}^{N-1} x(r_l, m) \exp(-j2\pi f_n 2r_l / c) \tag{4-3}$$

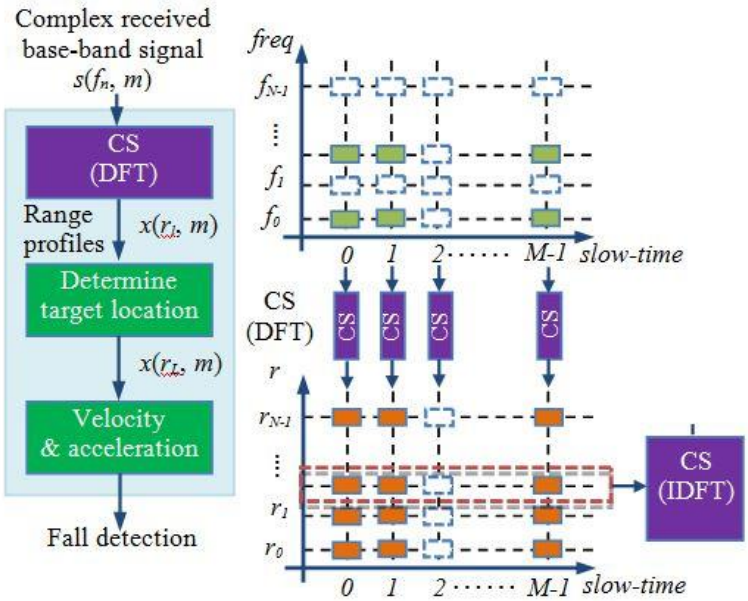
which can be rewritten in a matrix form as $s = \Phi_{DFT} \cdot x$, where s and x are the column vectors obtained by stacking $s(f_n)$ and $x(r_l)$, respectively. $\Phi_{DFT}(N \times N)$ is the measurement matrix where each element is defined as $\exp(-j \cdot 2\pi f_n \cdot 2r_l/c)$. In the CS-based approach, due to the sparseness of the target space, the baseband signals, s^{CS}, are measured at a random subset N^{CS} ($< N$) frequencies of the total bandwidth.

The reduced measurement matrix Φ_{DFT}^{CS} is constructed by randomly selecting N^{CS} rows of matrix Φ_{DFT}, i.e. corresponding to the selected frequencies. The reconstruction of the range profile is formulated as a convex optimization problem,

$$\hat{x} = \arg\min \|x\|_1 \quad s.t. \quad s = \Phi_{DFT} \cdot x \tag{4-4}$$



(a)



(b)

Figure 4.1. Fall detection monitoring using (a) conventional method and (b) compressive sensing.

We propose a two-step CS-based approach as illustrated in Figure 4.1. For each slow-time index, the complex received baseband signals, S^{CS}, are measured at a random subset M^{CS}($<M$) frequencies. Consequently, the reduced measurement matrix Φ_{DFT}^{CS} is constructed by randomly selecting M^{CS} rows from the full matrix Φ_{DFT}^{CS}. The reconstruction of the range profiles can be solved by using the well-known Orthogonal Matching Pursuit (OMP) algorithm. The procedure is repeated for random indices of slow-time during the entire observation duration. The Φ_{IDFT}^{CS} is constructed by randomly selecting N^{CS} rows Φ_{IDFT} from corresponding to random slow-time indices. The frequency spectrum of the breathing pattern then is recove red by using OMP algorithm. After the reconstruction process, the breathing signa l can be recalculated by the IDFT.

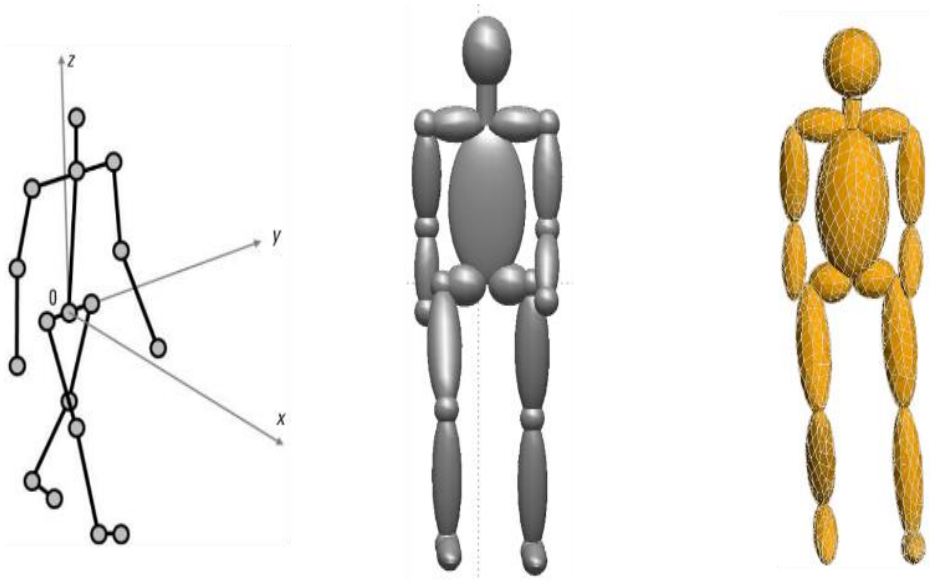
The reconstruction of the range profiles is solved by OMP algorithm. With the obtained range profiles, the critical information for fall detection, i.e. the velocity, acceleration and jerk of subjects, can be readily calculated. The relationship between the slow-time samples $x(r_l, m)$ at the range bin r_L corresponding to the target location and their Fourier transform $b(r_L)$ can be expressed in a matrix form as $x(r_L)=\Phi_{IDFT} \cdot b(r_L)$, where Φ_{IDFT} is the inverse discrete Fourier transform matrix. The procedure is repeated for random indices of slow-time during the entire observation duration. The measurement matrix Φ_{IDFT}^{CS} is constructed by randomly selecting M^{CS} ($<M$) rows from Φ_{IDFT} corresponding to random slow-time indices. The compressive sensing of SFCW radar for fall detection can be summarized and illustrated in Figure 4.1 (b).

The only limitation of the SFCW radar system is its high data acquisition time. Due to the sparsity of the range profile and the frequency domain data, a compressive sensing based approach was applied to reduce the data acquisition time. The CS algorithm was performed by randomly selecting 15 (30% of 50) frequency measurements. An example reconstruction result is shown Figure 4.1 where the simulation result of the CS based method shows good agreement with the conventional IFFT method for the case of a person falling on chair. The two-channel radar system shown in Figure 2.6 is used to demonstrate the viability of acquiring small amount of data for fall detection. Two horn antennas with 60cm transmitter-receiver spacing at a height of 110cm were used to collect the frequency domain measurements at frequencies from 2 GHz to 4 GHz with 20-MHz frequency steps. Hence, at each scan position and each channel, the SFCW can collect up to 50 frequency measurements. Furthermore, with CS we can get satisfactory results with 30% of total frequencies points. To the human motion characteristics of walking, limping and falling will be studied to validate the performance of radar using compressive sensing.

4.3 Full-wave electromagnetic scattering model

To validate the experimental results and provide a controlled environment to independently investigate the impact of different parameters, we utilize a full wave electromagnetic model for the human body and its different motions. First, we describe a full wave modeling approach, which requires creating and meshing the human body including all the joints that support a given motion. Then we describe our approach to dynamically move this human model to satisfy these different motions; namely falling, walking and limping.

For modeling the different body parts, the human body is represented by 17 ellipsoids. To model human motion kinematics, we utilize an analytical model extracted from empirical data, namely, the well-known Boulic model [56]. According to this model, human walking motion is modeled by cycles with constant translational velocity. There are two inputs to this model – velocity and height of the human. From these inputs, the human body phantom can be created using 16 joints between its 16 body parts, which are identified as the head and the lines between the joints, as depicted in Figure 4.2 (a). Furthermore, the fundamental spatial and temporal motion characteristics (i.e. the length of the walking cycle, L_c, and the duration of the walking cycle, T_c) are also determined from these inputs.



(a) (b) (c)

Figure 4.2. Human body (a) Human model with 17 joints, (b) Human models with 16 ellipsoids and (c) Meshed human body.

The time-dependent translation and rotation of each joint on a human body are then calculated using these two parameters, i.e. L_c and T_c. Figure 4.2 (b) shows the radial speeds of different human body parts for one walking cycle, T_c = 2.3 s, created by the Boulic model for a human of height 1.72 m, walking at 0.33 m/s speed. We can see that the lower parts of the legs such as the feet and the ankles achieve the maximum μ-D frequency at around 30 Hz, while the torso and hands oscillate slightly around the velocity of the translational movement of the human. The motions of the left and right parts of human body are observed to be periodic.

A full-wave technique, namely Method of Moments enhanced with Fast Multipole Method (MoM-FMM) is used to calculate the scattered fields from the human [56]. Mutual coupling effects between different body parts are computed accurately by using this method. Because the human is electrically large, parallelized implementation of MoM-FMM on a high-performance computing platform is performed to accelerate the computation time. MoM-FMM is an efficient numerical method, which relies on grouping sources over the scatterer according to their proximity to each other. It utilizes the concept of near and far field interactions, which significantly reduces the complexity of MoM from $O(N^3)$ to $O(N^{3/2})$, where N is the number of unknowns corresponding to the number of edges of the meshed object [37]. Implementing a parallelized version of this method on a high-performance computing (HPC) platform provides a good speedup factor for the computation time for large-scale scattering problems. The more information of the MoM-FMM can be found in A.3.

For the walking human scenario, the analytical Boulic model [56] is used to characterize the rotations and translations of each human body part over the duration of the walk. For the limping case, the rotation of one of the legs in the Boulic model is eliminated. For the falling scenario, the standing human model is rotated around one foot over the duration of the fall; i.e. until the head hits the floor.

4.4 Fall Detection Analysis

In this chapter, the human fall detection is presented using compressive sensing (CS) algorithm with stepped-frequency continuous wave radar (SFCW). In the proposed method, phase information of the high-resolution range profile (HRRP) was used to detect the motion characteristics of the human. There are distinct features of each activity that helps in distinguishing the respective events with a high degree of accuracy. The distinct events that are considered here in this research are regular activities such as standing and walking, limping and falling on a mattress. Promising results from both simulation and experiments demonstrate the applicability of the proposed system in speeding up the data acquisition process.

The two-channel radar system was used to demonstrate the viability of acquiring small amount of data for fall detection. Two horn antennas with 60cm transmitter-receiver spacing at a height of 110cm were used to collect the frequency domain measurements at frequencies from 2 GHz to 4 GHz with 20-MHz frequency steps. Hence, at each scan position and each channel, the SFCW can collect up to 50 frequency measurements. Furthermore, with CS we can get satisfactory results with 30% of total frequencies points. To classify the human motion characteristics of walking, limping and falling will be studied to validate the performance of radar using compressive sensing.

4.4.1 Standing and Walking

In the first scenario, a human stood-still at around 4 m away from the radar system for 5 seconds, and then walked about 2 m towards the radar. Figure 4.3 shows the velocity of the human walking with both simulation and conventional method. The range information of the human can be clearly seen in the HRRP in Figure 4.7 (a). it can be observed that the velocity changes significantly, as the target begins moving. While on movement, the velocity does not change too much, and after the target stops, the velocity goes back to zero again. Both experimental and simulation results show the average instantaneous velocity of human about 0.3 m/s which is close to the average velocity of the human. By using the proposed CS, we can acquire the instantaneous velocity of the human. When NCS=30% is performed on frequency samples, it is shown in Figure 4.3 that detected velocity of the CS-based method matches well with the one recovered with conventional method and simulation.

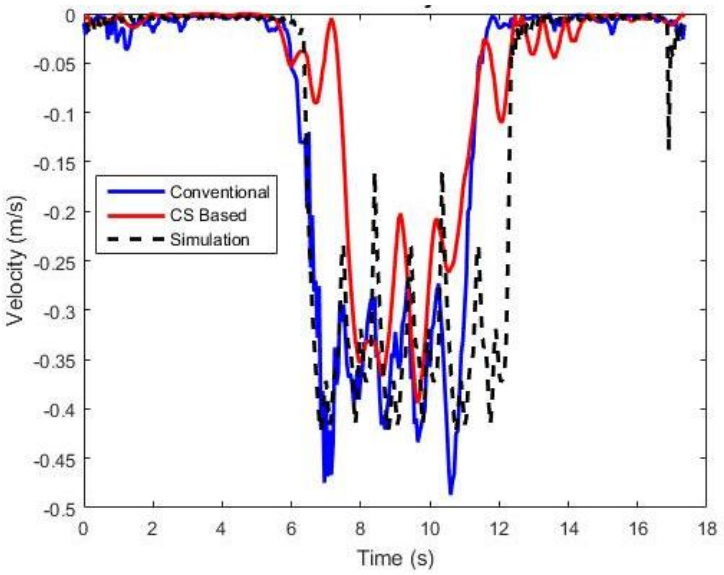


Figure 4.3. When subject walking, the instantaneous velocity acquired with simulation, conventional method and CS.

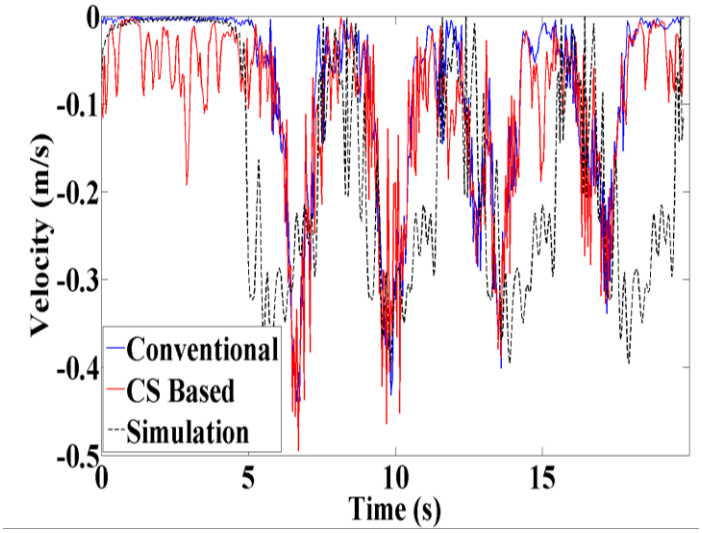


Figure 4.4. The velocity of the target limping obtained from experimental data and simulation.

4.4.2 Limping

For the limping event, human starts standing-still at 3.5 m away from the radar system, and then walks 2 m towards the radar. The range information of the human can be clearly seen in the HRRP as shown in Figure 4.4 shows too the velocity of the human subject limping. In both experiment and simulation, human subject is moving by dragging the right foot in 4 walking cycles. Figure 4.4 shows that the velocity jumps from 0.5 m/s to 0 m/s, and there is a good agreement between experimental and simulation results. Based on this feature, we can distinguish limping from regular walking. Again, the slight differences between experimental and simulation results as in the experiment, the second half of one walking cycle is longer that the first one; which is different from simulation as it is hard to emulate that exactly in real life. Figure 4.7 (b) and Figure 4.7 (e) show that the HRRP and the velocity of the proposed CS match well the experimental and the simulation results.

4.4.3 Falling on the ground

For a fall event, there is a sudden change in velocity where it reaches a peak then goes back to zero. In the third scenario, the subject stood-still and then fell on an air mattress on the ground. The target hit the mattress, then bounced up a little and fell down again and that is why two peaks with a near zero value in between are observed in the velocity data. Velocity, acceleration and jerk information of the subject falling on the ground obtained using both conventional method and compressive sensing are presented in Figure 4.5, 4.6 (a) and 4.6 (b) respectively. As seen from Figure 4.5, both experiment and simulation results show two peaks of the instantaneous velocity around 0.5 m/s and 0.58 m/s. By using the proposed

CS, we can achieve two peaks for velocity. The jerk data of both falling cases show magnitude of greater scale, which corroborates the falling event. The HRRP of subject acquired with conventional method is shown in Figure 4.7 (c). Based on the velocity and HRRP information, the falling of subject can be clearly distinguished from other activities, i.e. walking and limping.

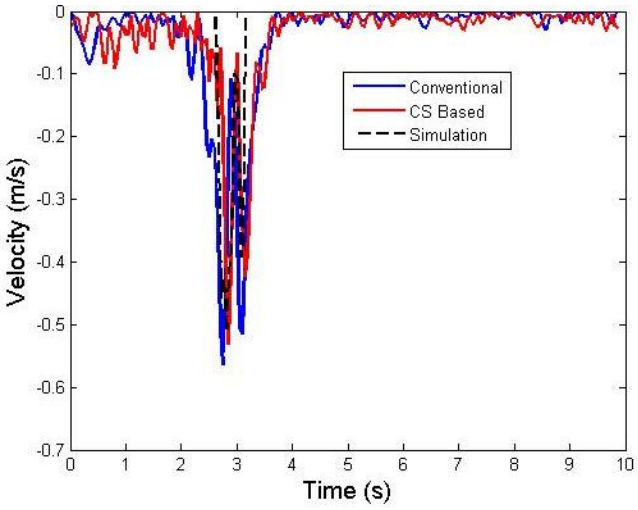
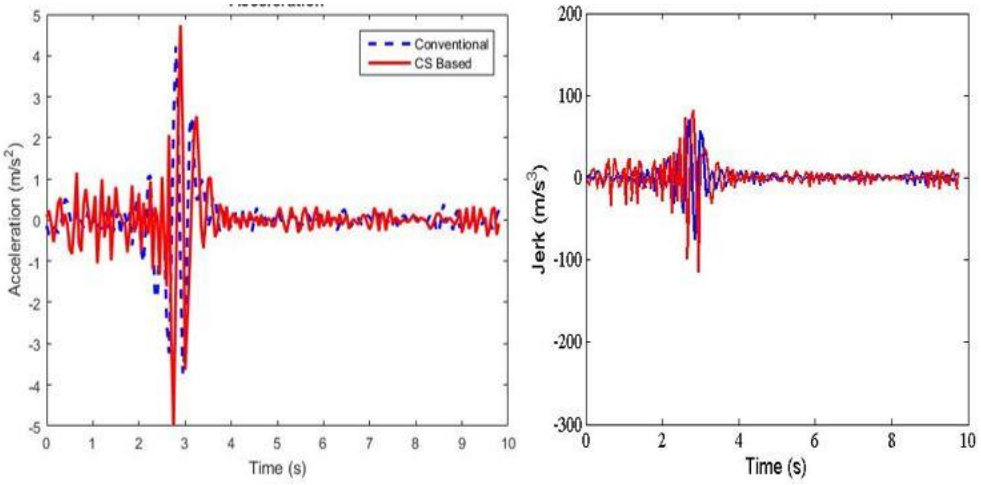


Figure 4.5. The velocity of the subject falling on mattress from a standing position obtained from experimental data (conventional/full set and CS) and from simulation.



(a) (b)

Figure 4.6. The target falling on a mattress from a standing position obtained from experimental data (conventional and CS) and from simulation, (a) acceleration, and (b) from experimental data using conventional method and CS.

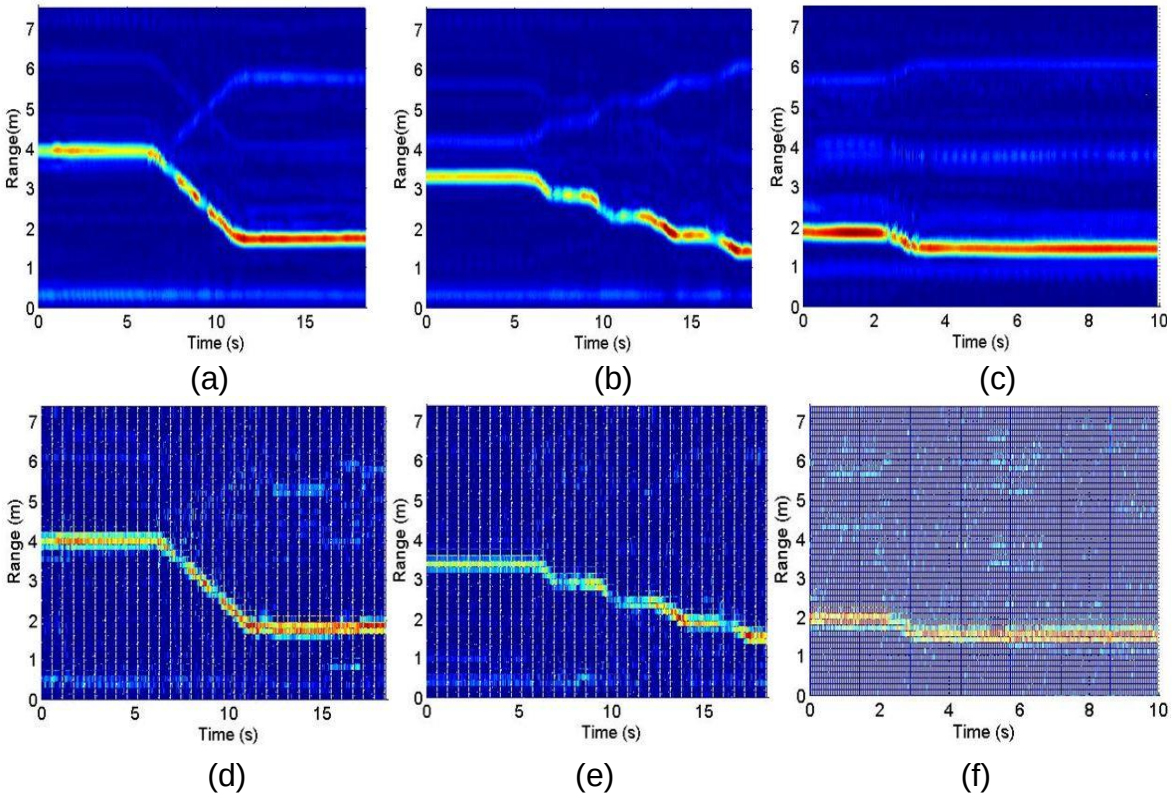


Figure 4.7. (a) HRRP for walking, (b) HRRP for limping, (c) HRRP for falling, (d) Walking HRRP using CS, (e) Limping HRRP using CS, (f) Falling HRRP using CS.

4.5 Conclusion

There is a need to simultaneously track activities of more than one patient almost 24/7. The amount of generated data is extremely huge and overwhelming. Doctors and nurses should only be notified with positive alarms. Hence, methods must be developed like SFCW radar instead of UWB radars to reduce the amount of acquired radar data. It was clear from the above experiments that using the HRRP, velocity and jerk information of fall events for example could be clearly detected with minimal false positives. Use of velocity, acceleration, and jerk could be used in identifying specific fall scenarios too. Along the same lines, we demonstrated that use of CS can drastically reduce the adequate data required to regenerate the events, good agreement was noted even for 30% of the full data set. Again, as soon as a fall event is detected, health care providers are required to be notified to reduce the subsequent adverse effects, but such implementation only requires handling of minimal amount of data.

CHAPTER FIVE

SUMMARY OF WORK

Radar technology is becoming popular nowadays and has been proposed for a variety of biomedical applications. Doppler, CW, UWB, and SFCW radars have been utilized extensively for vital signs monitoring of human body, penetrating through obstacles, high precision ranging at the centimeter level and patient motion monitoring. UWB radar, in particular, has been receiving attention lately for this application but its performance is limited by the complexity in designing the antenna, the power source and the method of dealing with electromagnetic interferences (EMI). Therefore, Stepped-frequency continuous wave radar (SFCW) is used to develop human non-contact vital signs detection due to its high signal-to-noise ratio, sensitivity and less stringent hardware requirements. The proposed SFCW radar can the human vital signs through obstacles and debris made of materials such as wood, plaster, rock, metal and concrete. The accuracy of the vital signs detection is proved to be less than 3% compare to electromagnetic model and contact sensors such as belt sensors and pulse sensors.

In addition, the SFCW can be extended to detect and eventually prevent elderly people falls; as injuries sustained from their fall incidents at home are considered the most dangerous cause of fatal accidents. Instant detection of fall events significantly lowers the mortality risk of the elderly people, which in turn enhances the feasibility of their independent living. The phase information of the high-resolution range profile (HRRP) is used to detect the motion characteristics of the human, which include the instantaneous velocity, acceleration and jerk i.e. the third derivative of position. Analyzing and combining this information can distinguish fall events accurately in comparison with regular activities such as standing, walking, limping and falling. It was observed that the fall events could be clearly detected with minimal false positives. Use of velocity, acceleration, and jerk could be used in identifying specific fall scenarios. Even the one disadvantage of the SFCW radar which is its high acquisition time can also be overcome using the concept CS. As soon as a fall event is detected in the actual implementation of the system in a real environment, health care providers are required to be notified to reduce the subsequent adverse effects.

In this effort, a single channel, multi-channel and finally a compact SFCW radar system were designed and implemented, which can transmit a set of frequencies simultaneously via one UWB antenna over multiple channels operating in parallel. In many applications, a hand-held radar system is desired. A Doppler radar at one frequency is adequate fr vital sign detection, while accurate localization capabilities can be achieved using the SFCW operation. The performance of the designed SFCW radar system has been evaluated and the applicability of this SFCW UWB

radar system, e.g., precise target localization, fall detection and vital sign detection has been investigated. Results from the experiments, wearable sensors, and EM modeling agree well. The developed model has proven to be accurate and can be extended to analyze various human activities including walking, fall events and eventually to other human activities including gait analysis for better understanding of motion kinematics.

The developed highly accurate EM model for the scenes include various human activities; so we can fine-tune our signal processing and hardware development in designing a proper radar system for human activity monitoring and detection. The developed EM model for heart rate and respiration rate detection accuracy has been validated and it approximates the torso by a homogenous equivalent dielectric layer, while utilizing an accelerated parallel version of the multi-level fast multipole algorithm to speed up the computation. Use of a parallel version of MLFMA implemented on GPU clusters led to pronounced speed acceleration.

The validated human vital signs EM model experimentally, the developed SFCW radar operating over 1 GHz bandwidth has been used for validation. SFCW radars are typically relatively easy to build and calibrate but newer generations of FMCW radars have been recently introduced and have addressed many of their known shortcomings like non-linearity and could even outperform SFCW performance and should be considered in future studies. Meanwhile, the results shown by our current model of the SFCW radar performance is accurate (the error rate is around 3%); when the subject is facing the radar and up to 1 m away from the radar. However, when the subject is farther away or at different angles facing the radar or there are multiple subjects in the scene, the performance could be slightly degraded due to reduced RCS or lower signal to noise ratios, and subsequently error goes up to 6%. The presence of more than one subject and in close proximity definitely causes pronounced interference and signal distortion.

Methods have been developed like SFCW radar instead of UWB radars to reduce the amount of acquired radar data. Given that there is a need to simultaneously track activities of more than one patient almost 24/7, which would produce large amount of data which could be extremely huge and overwhelming. Along the same lines, we have demonstrated that use of CS can drastically reduce the adequate data required to regenerate the events, good agreement was noted even for 30% of the full data set. Again, as soon as a fall event is detected, health care providers are required to be notified to reduce the subsequent adverse effects, but such implementation only requires handling of minimal amount of data.

5.1 Future Work

The SFCW radar system is implemented using commercial discrete components for vital signs detection and fall detection of elderly people. The next step of the SFCW radar implementation can be performed by designing individual component ICs in CMOS or GaAs process. Eventually, the whole system can be contained within a single chip. That can give us the freedom to construct the SFCW radar system at any frequency range with the desired system parameters in terms of noise figure and power levels. In addition, the SFCW radar system can be focused for other human sensing applications in future such as gait analysis and physical activity monitoring.

LIST OF REFERENCES

[1] Teng XF, Zhang YT, Poon CCY, Bonato P. Wearable medical systems for p-Health. IEEE Rev Biomed Eng 2008; 1:62-74.
[2] Topol EJ. Transforming medicine via digital innovation. Sci Transl Med 2010;2(16):1-3 7.
[3] Scanaill C, Carew S, Barralon P, et al. A review of approaches to mobility telemonitoring of the elderly in their living environment. Ann Biomed Eng 2006;4(4): 547-63 8.
[4] Baig MM, Gholamhosseini H, Connolly MJ. A comprehensive survey of wearable and wireless ECG monitoring systems for older adults. Med Biol Eng Comput 2013;51(5):485-95
[5] S. R. Lord, C. Sherrington, H. B. Menz, and J. C. Close, Falls in older people: risk factors and strategies for prevention: Cambridge University Press, 2007
[6] G. Vinci, S. Lindner, F. Barbon, S. Mann, M. Hofmann, A. Duda, R. Weigel, and A. Koelpin, "Six-port radar sensor for remote respiration rate and heartbeat vital-sign monitoring," *IEEE Trans. Microw. Theory Techn.*, vol. 61, no. 5, pp. 2093-2100, 2013.
[7] M.-C. Huang, J. J. Liu, W. Xu, C. Gu, C. Li, and M. Sarrafzadeh, "A self-calibrating radar sensor system for measuring vital signs," *IEEE Trans. Biomed. Cir. Syst.*, vol. 10, no. 2, pp. 352-363, 2016.
[8] H.-C. Kuo, C.-C. Lin, C.-H. Yu, P.-H. Lo, J.-Y. Lyu, C.-C. Chou, and H.-R. Chuang, "A fully integrated 60-GHz CMOS direct-conversion Doppler radar RF sensor with clutter canceller for single-antenna noncontact human vital-signs detection," *IEEE Trans. Microw. Theory Techn.*, vol. 64, no. 4, pp. 1018-1028, 2016.
[9] F. Quaiyum et al., “Development of a Reconfigurable Low Cost Multi-mode Radar System for Contactless Vital Signs Detection,” *IEEE MTT-S Int. Microw. Symp.*, Honolulu, HI, 2017, pp. 1245-1247.
[10] K. M. Chen, et al., “Microwave Life-detection Systems for Searching Human Subjects under Earthquake Rubble or Behind Barrier,” *IEEE Trans. Biomed. Eng.*, vol. 27, pp. 105-114, Jan. 2000.
[11] F. Quaiyum,et al., “Electromagnetic Modeling of Vital Sign Detection and Human Motion Sensing Validated by Noncontact Radar Measurements,” in IEEE Journal of Electromagnetics, RF and Microwaves in Medicine and Biology, vol. 2, no. 1, pp. 40-47, March 2018.
[12] J. E. Kiriazi, O. Boric-Lubecke, and V. M. Lubecke, “Dual-frequency technique for assessment of cardiopulmonary effective RCS and displacement,” *IEEE Sens. J.*, vol. 12, no. 3, pp. 574–582, Mar. 2012.
[13] R. Ricci, A. Balleri, “Recognition of Humans Based on Radar Micro-Doppler Shape Spectrum Features,”, *IET Radar Sonar Navigat.*, vol. 9, no. 9, pp. 1216-1223, Dec. 2015.
[14] G. Gennarelli, G. Ludeno, F. Soldovieri, “Real-time Through-wall Situation Awareness using a Microwave Doppler Radar Sensor,” *Remote Sens.*, vol. 8, no. 8, pp. 621, 2016.

[15] T. Fan et al., “Wireless Hand Gesture Recognition based on Continuous-wave Doppler Radar Sensors", *IEEE Trans. Microw. Theory Tech.*, vol. 64, no. 11, pp. 4012-4020, Oct. 2016.
[16] P. Bernardi, R. Cicchetti, S. Pisa, E. Pittella, E. Piuzzi, and O. Testa, "Design, realization, and test of a UWB radar sensor for breath activity monitoring," *IEEE Sensors Journal,* vol. 14, no. 2, pp. 584-596, 2014.
[17] J. C. Y. Lai, Y. Xu, E. Gunawan, E. C.-P. Chua, A. Maskooki, Y. L. Guan, K.-S. Low, C. B. Soh, and C.-L. Poh, "Wireless sensing of human respiratory parameters by low-power ultrawideband impulse radio radar," *IEEE Transactions on Instrumentation and Measurement,* vol. 60, no. 3, pp. 928-938, 2011.
[18] X. Wang, A. Dinh, and D. Teng, "3-10 GHz ultra wideband front-end transceiver in 0.13 μm complementary metal oxide semiconductor for low-power biomedical radar," *IET Circuits, Devices & Systems,* vol. 8, no. 4, pp. 272-279, 2014.
[19] K. K.-M. Chan, A. E.-C. Tan, and K. Rambabu, "Circularly polarized ultra-wideband radar system for vital signs monitoring," *IEEE Transactions on microwave theory and techniques,* vol. 61, no. 5, pp. 2069-2075, 2013.
[20] B. Schleicher, I. Nasr, A. Trasser, and H. Schumacher, "IR-UWB radar demonstrator for ultra-fine movement detection and vital-sign monitoring," *IEEE Trans. Microw. Theory Techn.,* vol. 61, no. 5, pp. 2076-2085, 2013.
[21] D. Zito, D. Pepe, M. Mincica, F. Zito, A. Tognetti, A. Lanatà, and D. De Rossi, "SoC CMOS UWB pulse radar sensor for contactless respiratory rate monitoring," *IEEE Transactions on Biomedical Circuits and Systems,* vol. 5, no. 6, pp. 503-510, 2011.
[22] G. Wang, C. Gu, T. Inoue, and C. Li, "A hybrid FMCW-interferometry radar for indoor precise positioning and versatile life activity monitoring," *IEEE Transactions on Microwave Theory and Techniques,* vol. 62, no. 11, pp. 2812-2822, 2014.
[23] S. Wang, A. Pohl, T. Jaeschke, M. Czaplik, M. Köny, S. Leonhardt, and N. Pohl, "A novel ultra-wideband 80 GHz FMCW radar system for contactless monitoring of vital signs," in *IEEE Engineering in Medicine and Biology Society (EMBC)*, Milan, Italy, 2015, pp. 4978-4981.
[24] G. Wang, J.-M. Munoz-Ferreras, C. Gu, C. Li, and R. Gomez-Garcia, "Application of linear-frequency-modulated continuous-wave (LFMCW) radars for tracking of vital signs," IEEE Transactions on Microwave Theory and Techniques, vol. 62, no. 6, pp. 1387-1399, 2014.
[25] M. Mercuri, P. J. Soh, G. Pandey, P. Karsmakers, G. A. Vandenbosch, P. Leroux, and D. Schreurs, "Analysis of an indoor biomedical radar-based system for health monitoring," IEEE Trans. Microw. Theory Techn., vol. 61, no. 5, pp. 2061-2068, 2013.
[26] L. Qiu, T. Jin, B. Lu and Z. Zhou, “An Isophase-Based Life Signal Extraction in Through-the-Wall Radar,” in IEEE Geoscience and Remote Sensing Letters, vol. 14, no. 2, pp. 193-197, Feb. 2017.

[27] L. Ren, H. Wang, K. Naishadham, Q. Liu, and A. E. Fathy, "Non-invasive detection of cardiac and respiratory rates from stepped frequency continuous wave radar measurements using the state space method," in *IEEE MTT-S International Microwave Symposium (IMS)*, Phoenix, AZ, USA, 2015, pp. 1-4.

[28] L. Liu and S. Liu, "Remote detection of human vital sign with stepped-frequency continuous wave radar," *IEEE J. Sel. Topics Appl. Earth Observ. in Remote Sens.,* vol. 7, no. 3, pp. 775-782, 2014.

[29] Z. Peng et al., “A Portable FMCW Interferometry Radar With Programmable Low-IF Architecture for Localization, ISAR Imaging, and Vital Sign Tracking,” in IEEE Transactions on Microwave Theory and Techniques, vol. 65, no. 4, pp. 1334-1344, Apr. 2017.

[30] H. Wang, V. Dang, L. Ren, Q. Liu, L. Ren, E. Mao, O. Kilik, and A. E. Fathy, "An elegant solution: an alternative ultra-wideband transceiver based on stepped-frequency continuous-wave operation and compressive sensing," IEEE Microwave Magazine, vol. 17, no. 7, pp. 53-63, 2016.

[31] A. De Leo, V. Petrini, P. Russo, et al., “An EM Modeling for Rescue System Design of Buried People,” International Journal of Antennas and Propagation, vol. 2015, Article ID 465651, 7 pages, 2015. doi:10.1155/2015/465651.

[32] C. Li and J. Lin, “Random Body Movement Cancellation in Doppler Radar Vital Sign Detection,” in IEEE Transactions on Microwave Theory and Techniques, vol. 56, no. 12, pp. 3143-3152, Dec. 2008.

[33] R. Neely, K. Naishadham, A. Sharma and K. Bing, “Electromagnetic human body modeling with physiological motion for radar applications,” 2012 IEEE Radar Conference, Atlanta, GA, 2012, pp. 0818-0823.

[34] V. Dang, T. Phan and O. Kilic, “Compressive sensing based approach for detection of human respiratory rate,” 2015 IEEE International Symposium on Antennas and Propagation & USNC/URSI National Radio Science Meeting, Vancouver, BC, 2015, pp. 394-395.

[35] F. Bellemare, A. Jeaneret, and J. Couture, “Sex differences in thoracic dimensions and configuration,” Am J Respir Crit Care Med, vol. 168, pp. 305-312, May 2003.

[36] A. Lazaro, D. Girbau, and R. Villarino, “Analysis of vital signs monitoring using an IR - UWB radar,” Progress In Electromagnetics Research, vol. 100, 265-284, 2010.

[37] C Gabriel, S Gabriel and E Corhout, “The dielectric properties of biological tissues: I. Literature survey” in Phys. Med. Biol, vol 41, pp.2231 – 2249, UK, 1996.

[38] J. Kennedy and R. Eberhart, “Particle swarm optimization,” Proceedings of the IEEE International Conference on Neural Networks, Perth, WA, 1995, pp. 1942-1948, vol. 4.

[39] J. Robinson and Y. Rahmat-Samii, “Particle swarm optimization in electromagnetics,” in IEEE Transactions on Antennas and Propagation, vol. 52, no. 2, pp. 397-407, Feb. 2004.
[40] L. Ren, H. Wang, K. Naishadham, O. Kilic and A. E. Fathy, “Phase-Based Methods for Heart Rate Detection Using UWB Impulse Doppler Radar,” in IEEE Transactions on Microwave Theory and Techniques, vol. 64, no. 10, pp. 3319-3331, Oct. 2016.
[41] K. Naishadham, J. E. Piou, L. Ren and A. E. Fathy, “Estimation of Cardiopulmonary Parameters From Ultra Wideband Radar Measurements Using the State Space Method,” in IEEE Transactions on Biomedical Circuits and Systems, vol. 10, no. 6, pp. 1037-1046, Dec. 2016.
[42] L. Ren, Y. S. Koo, Y. Wang, and A. E. Fathy, "Noncontact heartbeat detection using UWB impulse doppler radar," in IEEE Topical Conference on Biomedical Wireless Technologies, Networks, and Sensing Systems (BioWireleSS), 2015, pp. 1-3.
[43] H. Samet, “An Overview of Quadtrees, Octrees, and Related Hierarchical Data Structures,” In: Earnshaw R.A. (eds) Theoretical Foundations of Computer Graphics and CAD. NATO ASI Series (Series F: Computer and Systems Sciences), vol 40. Springer, Berlin, Heidelberg.
[44] T. Phan, N. Tran and O. Kilic, “Multi-level Fast Multipole Algorithm for 3-D Homogeneous Dielectric Objects Using MPI-CUDA on GPU Cluster”, Applied Computational Electromagnetics Society Express Journal, Vol.1, no .8, pp. 216-219, Aug. 2016.
[45] L. Ren, Y. S. Koo, H. Wang, Y. Wang, Q. Liu and A. E. Fathy, “Noncontact Multiple Heartbeats Detection and Subject Localization Using UWB Impulse Doppler Radar,” in IEEE Microwave and Wireless Components Letters, vol. 25, no. 10, pp. 690-692, Oct. 2015.
[46] S. R. Lord, C. Sherrington, H. B. Menz, and J. C. Close, Falls in older people: risk factors and strategies for prevention: Cambridge University Press, 2007.
[47] X. Yu, "Approaches and principles of fall detection for elderly and patient," in e-health Networking, Applications and Services, 2008. HealthCom 2008. 10th International Conference on, 2008, pp. 42-47.
[48] M. Alwan, P. J. Rajendran, S. Kell, D. Mack, S. Dalal, M. Wolfe, et al., "A smart and passive floor-vibration based fall detector for elderly," in Information and Communication Technologies, 2006. ICTTA'06. 2nd, 2006, pp. 1003-1007.
[49] Y. Li, Z. Zeng, M. Popescu, and K. Ho, "Acoustic fall detection using a circular microphone array," in Engineering in Medicine and Biology Society (EMBC), 2010 Annual International Conference of the IEEE, 2010, pp. 2242-2245.

[50] A. Mihailidis, B. Carmichael, and J. Boger, "The use of computer vision in an intelligent environment to support aging-in-place, safety, and independence in the home," Information Technology in Biomedicine, IEEE Transactions on, vol. 8, pp. 238-247, 2004.
[51] L. Liu, M. Popescu, K. Ho, M. Skubic, and M. Rantz, "Doppler radar sensor positioning in a fall detection system," in Engineering in Medicine and Biology Society (EMBC), 2012 Annual International Conference of the IEEE, 2012, pp. 256-259.
[52] M. Wu, X. Dai, Y. D. Zhang, B. Davidson, M. G. Amin, and J. Zhang, "Fall detection based on sequential modeling of radar signal time-frequency features," in Healthcare Informatics (ICHI), 2013 IEEE International Conference on, 2013, pp. 169-174.
[53] M. Mercuri, D. Schreurs, and P. Leroux, "SFCW microwave radar for in-door fall detection," in Biomedical Wireless Technologies, Networks, and Sensing Systems (BioWireleSS), 2012 IEEE Topical Conference on, 2012, pp. 53-56.
[54] M. Mercuri, P. J. Soh, G. Pandey, P. Karsmakers, G. A. Vandenbosch, P. Leroux, et al., "Analysis of an indoor biomedical radar-based system for health monitoring," Microwave Theory and Techniques, IEEE Transactions on, vol. 61, pp. 2061-2068, 2013.
[55] H. Wang, L. Ren, E. Mao, and A. E. Fathy, "Phase based motion characteristics measurement for fall detection by using stepped-frequency continuous wave radar," in 2016 IEEE Topical Conference on Biomedical Wireless Technologies, Networks, and Sensing Systems (BioWireleSS), 2016, pp. 43-45.
[56] Boulic, Ronan, Nadia Magnenat Thalmann, and Daniel Thalmann. "A global human walking model with real-time kinematic personification." The visual computer 6.6 (1990): 344-358.

APPENDIX

A.1 DDS-Driven PLL Architecture

In the proposed two-channel SFCW radar system (as shown in figure 2.6), all the components are off-the shelf modules except for the DDS board. In this section, we present some design details of the developed DDS board. The conventional DDS consists of a phase accumulator, a sine waveform lookup table (LUT), a digital-to analog convertor (DAC), and a low-pass filter (LPF), as shown in figure A.1.1. The output frequency of the DDS is given by

$$f_{out} = \frac{F}{2\mathrm{I}} f_{clk} \tag{A1-1}$$

where *F* is the frequency-control word with I-b width and *fclk* is the frequency of the DDS system clock. Typically, the phase accumulator is truncated to reduce power dissipation and the die area. This truncation mechanism introduces a series of spurious components and degrades the spectral purity of the DDS output spectra. The truncation-resultant spur levels can be lowered by extending the bit width of F and the phase-accumulator output. In practical systems, there should be a tradeoff between spur levels and device complexity. We choose here the Analog Devices AD9914, which can achieve 64-b-width fine-tuning resolution using a programmable modulus mode for generating the stepped-frequency signal. Besides the truncation-resultant spurs, DAC images may introduce even higher spurs on the DDS output frequency spectra (i.e., image frequencies). The worst-case spurs occur when the images of the DAC harmonics fold back such that they are close to the DAC's fundamental frequency. The frequency of DAC images is:

$$F_{image} = Qf_{clk} \pm Tf_{out} \tag{A1-2}$$

where *Q* and *T* are integer multiples of *fclk* and *fout*, respectively. In the design, the DDS's output frequency is carefully chosen using an effective frequency planning method. With this method, the worst DAC images are placed well off from the DDS output frequency and are attenuated by a bandpass filter. The developed two-channel DDS board is shown in figure A.1.2. The two AD9914 chips can be configured with different waveform parameters using an Altera CPLD.

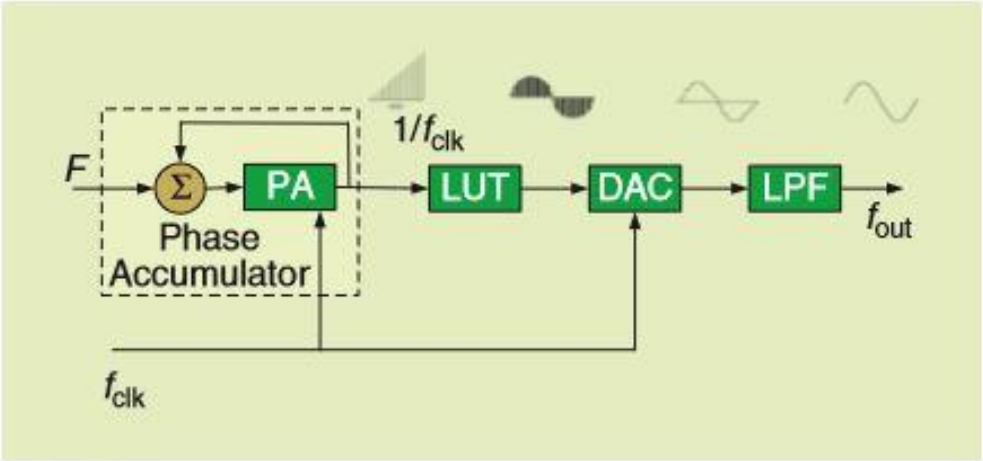


Figure A.1.1. The block diagram of a DDS, illustrating the output of each stage.

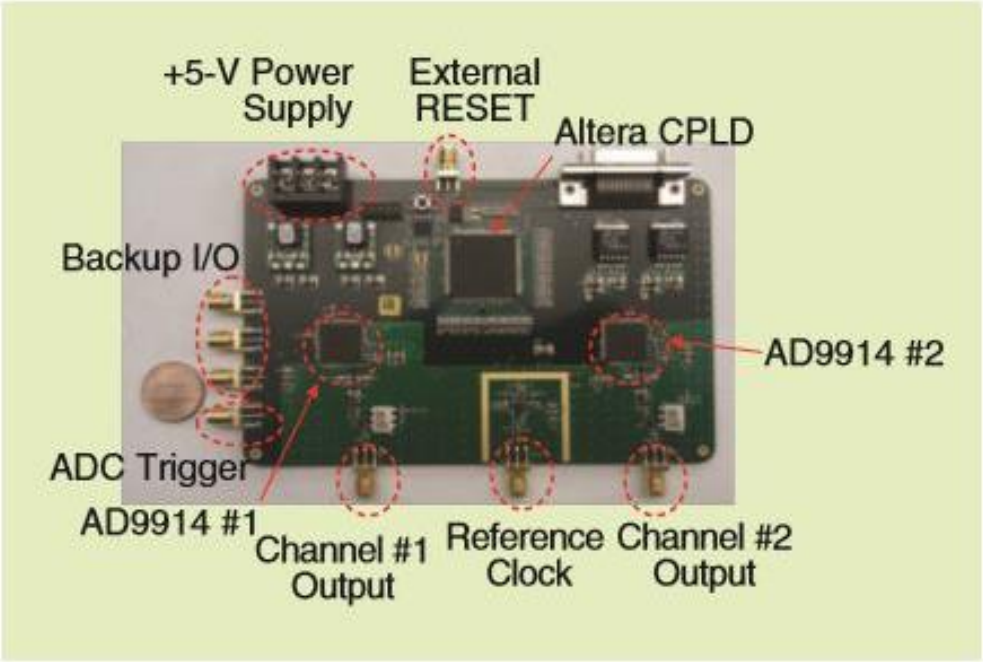


Figure A.1.2. A photograph of the two-channel DDS board.

A.2 Multi-level Fast Multipole Algorithm

There are various numerical techniques to compute the EM scattered fields for the complex structure depicted in Figure A.2.1, which distorts an elliptical cylinder surface periodically in time to emulate heartbeat and respiration motion impacts on the torso surface. Method of moments (MoM) is a well-known full wave EM frequency domain technique that relies on a fine triangular mesh of an arbitrary structure. For good accuracy, the mesh size is typically a small fraction of a wavelength "λ", i.e. λ/10. MoM creates a matrix equation in the form of ZI=V, where N is the number of edges in the mesh, Z is the N×N impedance matrix, I is the unknown currents represented by a vector of size N, and V is a known vector based on the incident fields at each mesh. Each element in the Z matrix represents the interactions between the currents along the different edges. An inverse matrix operation; i.e. a matrix vector product of Z-1 and V needs to be carried out for a solution in MoM, resulting in a complexity of O(N3). As a result, for electrically large objects MoM becomes prohibitive due to its memory requirements.

Numerous techniques have been developed to compliment MoM to reduce its computational complexity for large scale problems. For instance, while the conventional MoM accounts for all possible interactions among the edges, fast multipole algorithm (FMA) and multi-level fast multipole algorithm (MLFMA) are both based on a grouping concept, which reduces the complexity of computations in MoM. Both algorithms split the Z matrix into two groups; namely Znear and Zfar, based on the proximity among different groups (i.e. near and far groups). The fast multipole algorithm (FMA) defines this division based on spatial proximity of the edges and uses an approximate multiple expansion of the fields between near and far group to accelerate the matrix-vector product computations reducing the complexity to O(N3/2). The multi-level fast multipole algorithm (MLFMA) forms a hierarchical grouping structure instead; to render efficient interactions with far groups based on an Oct-tree structure to organize the N edges into an M-level tree structure; thus further reducing the complexity to O(NlogN). At level 0, the entire object is boxed by a cube. For the next level, the cube is divided into 8 equal smaller sub-cubes. The process of division into smaller cubes is iterated at each level until the cube size reaches about 0.3λ.

MLFMA has been successfully implemented by numerous authors on CPU clusters. Although such implementations take advantage of the large memory resources of CPU clusters, their speed in solving for the scattered fields for multiple frequencies and multiple time frames cannot match that of GPUs. In this work, we implement MLFMA on our GPGPU cluster platform using CUDA programming to leverage from both inherent parallel structure and fast computation time of GPGPUs. By definition, level 0 and level 1 of the Oct-tree structure have only near groups. MLFMA starts from level 2 which might have both near and far groups. While the pre-processing and post-processing stages which include geometry

mesh data reading, Oct-tree structure building, scattered fields calculation are performed on CPU, the most time consuming part, i.e. the processing stage, is handled by GPUs. This stage is comprised of three components: aggregation (radiation functions, interpolation), translation and disaggregation (receive function, anterpolation). The general process of MLFMA is shown in Figure A.2.1. To fully utilize all the computing nodes, the workload is distributed equally among them, and the inter-node communication is minimized. Within each node, two parallelization models can be utilized, namely parallel computing platform CUDA thread-block model [20] and p-threads models to calculate the workloads assigned to the node.

In our implementation, we employ a cluster with 13 computing nodes, which utilizes a dual 6-core 2.66 GHz CPU with 48 GB RAM in addition to NVidia Tesla M2090 GPUs at 1.3 GHz with 6 GB memory. The nodes are interconnected through Infiniband. The cluster populates the Native POSIX Thread Library (NPTL) 2.5, CUDA v6.0, and MVAPICH2 v1.8.1.

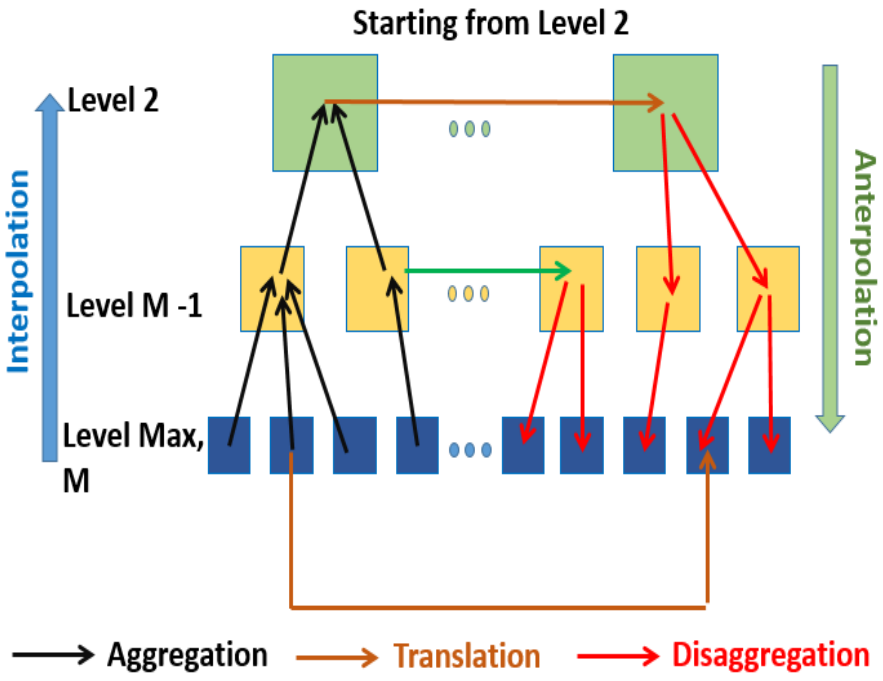


Figure A.2.1. The general process of MLFMA.

A.3 The detection algorithm for human activities using a human scattering model

MoM-FMM is an efficient numerical method, which relies on grouping sources over the scatterer according to their proximity to each other. It utilizes the concept of near and far field interactions, which significantly reduces the complexity of MoM from O(N3) to O(N3/2), where N is the number of unknowns corresponding to the number of edges of the meshed object. Implementing a parallelized version of this method on a high-performance computing (HPC) platform provides a good speedup factor for the computation time for large-scale scattering problems. A brief discussion on the parallel implementation of MoM-FMM on a GPU cluster is provided in the following section.

Full wave approach

In FMM, the linear equation system ZI = V is solved to find the unknown current I, where Z is the impedance matrix and V depends on the incident fields. Using the grouping concepts, M localized groups are created from the N edges in the mesh of a given structure based on their proximity. Two interaction types are defined: near and far. Subsequently the impedance matrix Z is split into two components, Znear and Zfar. The near interactions consist of interactions between spatially close edges and are computed using the conventional method- MoM. The remaining edges constitute the far term. For far terms, the radiation, receive and translations functions are computed based on electric field integral equation (EFIE) formulation. Typically, the right-hand side V vector is a simple calculation, and iterative methods are used to determine the unknown current I.

Parallelization on GPGPU Based HPC Platform

To speed up the computation, FMM is implemented on a Graphical Processing Unit (GPU) cluster. The geometry mesh and localized groups are read first to the GPU memory, second parallel implementation on GPU clusters is performed to compute the near interaction, the radiation/ received functions, the translation matrix and the V vector. Meanwhile, a biconjugate gradient stabilized method (BiCGSTAB) is implemented to solve the linear system iteratively. For workload distribution, the M groups are initially distributed uniformly among the computing nodes and computations are parallelized among computing nodes using MPI library. Followed by using CDUA programming model to distribute computations among various GPUs per computing nodes. In each node, the workload assigned to that node is computed using CUDA thread-block model.

Modeling Different Human Motions

In this paper, three human motions are simulated, namely falling, walking and limping to clearly show the distinct features of a falling case. In these three motions, the height of a human is the only input needed to create the human joints and body parts, similar to the assumptions employed in the Boulic model. The motion

characteristic for all joints are based on the average velocity as the human goes through the different motions investigated.

a) Falling on Knee

In the first scenario, the falling motion is modeled by rotating the joints of the standing human model around the ankles over the duration of the fall event until the human knees hit the floor. Initially, the human stood 4 m away from the radar system for 2 seconds, then completed the falling motion over 2 seconds, and stayed steady for 6 seconds as shown in Figure A.3.1.

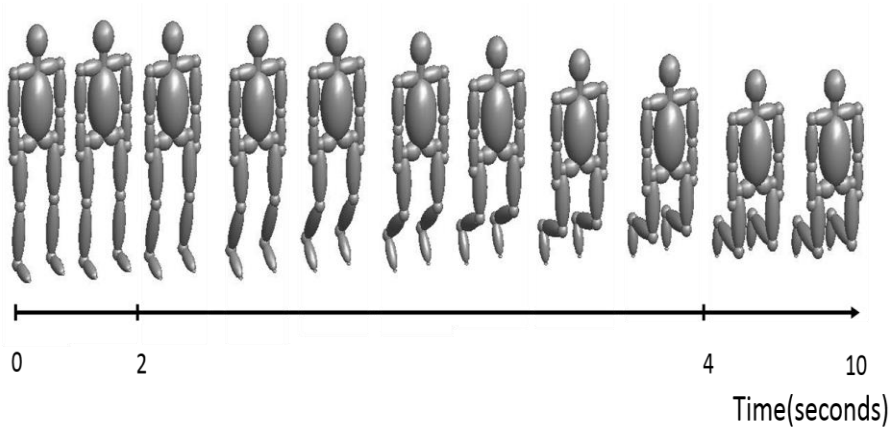


Figure A.3.1. Human motions: standing still and then falling on knee.

b) Walking

The regular walking motion is described using the analytical Boulic model based on time-dependent translations and rotations of each joint. The motion is characterized by cycles that repeat with a constant velocity. For this scenario, the human initially stood 4 m away from the radar system for 7 seconds, then walked towards the radar about 3 walking cycles for 6 seconds with an average velocity of 0.33 m/s, and finally paused still for 4 seconds as depicted in Figure A.3.2.

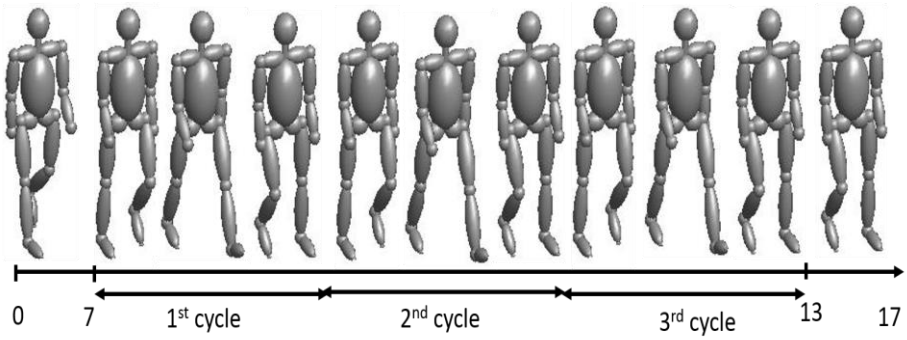


Figure A.3.2. Human motions: standing still and then walking.

c) Limping

In the third scenario, the Boulic model is modified such that the right foot of the human is dragged on the ground and the torso is rotated towards wherever the right foot is dragged to emulate a realistic scenario. For the limping event, human started standing still at 3.5 m away from the radar system for 3 seconds, then limped towards the radar for 8 seconds and finally stood for 9 seconds as shown in Figure A.3.3.

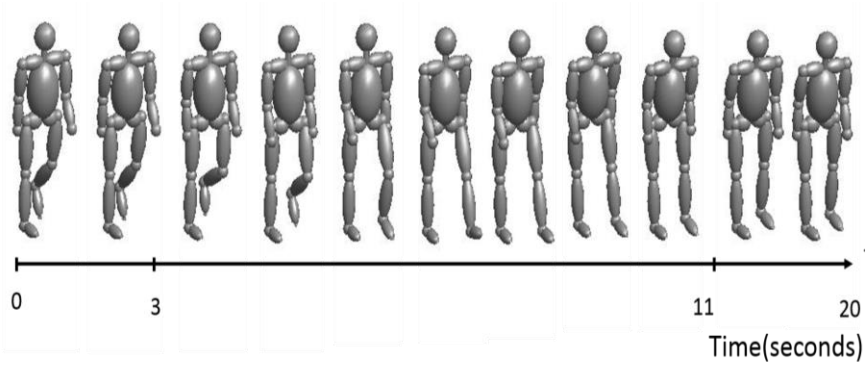


Figure A.3.3. Human motions: standing still and then limping.

VITA

Sabikun Nahar received her B.Sc. Degree in Electrical Engineering from Independent University, Bangladesh in 2012 where she worked on implementing a micro-computer using VHDL. In 2016, she joined the University of Tennessee as a graduate research assistant and started working on SFCW radar system and antenna design. She had several years of experience serving as a teaching assistant and industrial internee in the area of RF/Microwave circuit design. Her research interests include microwave antennas/circuits, stretchable bio-sensors, radar system design, RFIC/MMIC, and high efficiency power amplifier. She received her Master's degree in electrical engineering (with a focus on biomedical applications of microwave/RF systems and microwave circuit design) at the University of Tennessee, Knoxville, in 2018.